TU Delft

Delft University of Technology

Document Version
Final published version

Licence
Dutch Copyright Act (Article 25fa)

Citation (APA)
Gu, C., Hu, X., Lu, K., Wang, T., Yan, X., Chen, W., Chen, J., Fan, X., Zhang, G., & Fan, J. (2026). Revealing thermo-mechanical degradation mechanism of sintered silver nanoparticles under thermal shock via microstructure characterization and kinetic Monte Carlo simulation. *Materials Science and Engineering: A*, *953*, Article 149646. https://doi.org/10.1016/j.msea.2025.149646

Important note
To cite this publication, please use the final published version (if applicable).
Please check the document version above.

Copyright
In case the licence states “Dutch Copyright Act (Article 25fa)”, this publication was made available Green Open Access via the TU Delft Institutional Repository pursuant to Dutch Copyright Act (Article 25fa, the Taverne amendment). This provision does not affect copyright ownership.
Unless copyright is transferred by contract or statute, it remains with the copyright holder.

Sharing and reuse
Other than for strictly personal use, it is not permitted to download, forward or distribute the text or part of it, without the consent of the author(s) and/or copyright holder(s), unless the work is under an open content license such as Creative Commons.

Takedown policy
Please contact us and provide details if you believe this document breaches copyrights.
We will remove access to the work immediately and investigate your claim.

This work is downloaded from Delft University of Technology.

Green Open Access added to TU Delft Institutional Repository
as part of the Taverne amendment.

More information about this copyright law amendment
can be found at https://www.openaccess.nl.

Otherwise as indicated in the copyright section:
the publisher is the copyright holder of this work and the
author uses the Dutch legislation to make this work public.

Materials Science & Engineering A 953 (2026) 149646

Contents lists available at ScienceDirect

Materials Science & Engineering A

journal homepage: www.elsevier.com/locate/msea

Revealing thermo-mechanical degradation mechanism of sintered silver nanoparticles under thermal shock via microstructure characterization and kinetic Monte Carlo simulation

Chao Gu [a], Xiao Hu [b], Kai Lu [d], Tao Wang [d], Xuyang Yan [a], Wei Chen [a], Junwei Chen [a], Xuejun Fan [c], Guoqi Zhang [b], Jiajie Fan [a,b,e,*]

[a] Shanghai Engineering Technology Research Center of SiC Power Device, College of Intelligent Robotics and Advanced Manufacturing, Fudan University, Shanghai, 200433, China
[b] EEMCS Faculty, Delft University of Technology, Delft, 2628, the Netherlands
[c] Department of Mechanical Engineering, Lamar University, PO Box 10028, Beaumont, TX, 77710, USA
[d] Suzhou XiZ-Tech Co., Ltd. Suzhou 215000, China
[e] Research Institute of Fudan University in Ningbo, Ningbo, 315336, China

ARTICLE INFO

Keywords:
Sintered Ag nanoparticles
Degradation mechanisms
Microstructure evolution
Thermal shock
Kinetic Monte Carlo

ABSTRACT

Although silver sintering is widely used in die attach, its reliability under low-pressure and pressureless sintering conditions remains a challenge, and the degradation mechanism needs to be addressed urgently. This study investigates the degradation mechanisms of silver sintered die attach subjected to thermal shock (TS) (−45 °C to 125 °C), revealing its microstructural evolution, degradation of mechanical properties, and pore dynamics. After 1500 cycles, the average porosity did not decrease and remained at approximately 10%, but the porosity distribution exhibited significant heterogeneity, forming three characteristic regions of high porosity, low porosity, and crack regions. With the porosity evolution, the grain size increased by a factor of 2.1–2.8, with the largest grain sizes in the crack region, and the recrystallization fraction decreased significantly, from 89.6 % to a range of 37.3 %–72.1 %. Additionally, the combination with the decrease in both statistically stored dislocation density and total dislocation density reveals a decline in hardness and yield strength of silver sintered layer from 1.05 GPa and 326 MPa to 0.92 GPa and 231 MPa, respectively, gradually diminishing their ability to impede pore migration and merging. Thermal-mechanical coupling simulations based on the actual porous structure images show that the mismatch in the coefficient of thermal expansion induces alternating tensile and compressive thermal stresses, driving pore evolution and crack propagation. The kinetic Monte Carlo (KMC) Potts model based on Kawasaki dynamics combined with pore conservation can effectively predict the long-term pore evolution in this case. These findings provide important guidance for optimizing the sintering process and improving the application of silver sintering materials in high-reliability electronic packaging.

1. Introduction

To reduce the dependence on fossil energy, combat global warming, and drive the transition to a green and low-carbon economy, new energy vehicles, such as hybrid and electric vehicles, have developed rapidly worldwide [1,2]. As a core component in these vehicles, traction inverters increasingly adopt silicon carbide (SiC) metal-oxide-semiconductor field-effect transistors (MOSFETs), benefiting from the superior properties of wide-bandgap semiconductors, including higher thermal conductivity, wider bandgap, and lower power loss [3–5]. However, realizing the full potential and long-term reliability of SiC devices requires highly robust die-attach materials. Traditional Sn-based solders fall short under demanding conditions due to low melting points, poor thermal conductivity, and intermetallic compound formation. In contrast, silver (Ag) sintering technology has emerged as a promising solution to meet the high-reliability requirements of SiC dies [6–8].

Among die-attach solutions, silver sintering is widely adopted over

* Corresponding author. Shanghai Engineering Technology Research Center of SiC Power Device, College of Intelligent Robotics and Advanced Manufacturing, Fudan University, Shanghai, 200433, China.
E-mail address: jiajie_fan@fudan.edu.cn (J. Fan).

https://doi.org/10.1016/j.msea.2025.149646
Received 9 April 2025; Received in revised form 12 December 2025; Accepted 16 December 2025
Available online 2 January 2026
0921-5093/© 2026 Elsevier B.V. All rights are reserved, including those for text and data mining, AI training, and similar technologies.

copper sintering due to its superior oxidation resistance and process stability [9]. However, while pressure-assisted silver sintering offers reliable performance, it introduces design constraints, such as increased mechanical stress on the die and substrate, often mitigated by costly and complex intermediary layers like graphite sheets. As a result, pressureless silver sintering has attracted significant attention for simplifying processes and reducing costs. Nevertheless, its reliability remains limited by failure modes like die-attach layer delamination, which prevent compliance with industry standards such as AQG324 [10,11]. Thermal shock (TS) testing is critical for evaluating the reliability of sintered layers by simulating operational temperature cycles [12]. Due to mismatches in the coefficients of thermal expansion (CTE) between different materials, repeated thermal cycling induces thermal stress, leading to delamination, crack propagation, and eventual device failure [13,14]. Understanding the degradation mechanisms of sintered layers under TS is therefore essential to improving the reliability of both pressure-assisted and pressureless sintering technologies.

Previous studies have investigated the degradation behavior of silver sintered layers under various conditions, including high-temperature storage (HTS), thermal cycling (TC), and TS [15–17]. These studies highlight key degradation phenomena, such as porosity evolution, interfacial oxidation, and mechanical weakening. For instance, void growth during HTS reduces joint strength [15], while TS testing consistently leads to increased porosity and declining shear strength [16,18–20]. However, existing research often relies on localized porosity statistics and lacks comprehensive analysis of porosity evolution across entire sintered layers. Moreover, the shape and distribution of pores significantly influence failure behavior, with larger, irregular pores accelerating crack initiation and propagation. It can be attributed to two main failure mechanisms: the formation of edge cracks (which propagate along the crack tip) and the growth of the pores [17]. It has also been found that rectangular pores, compared to arc-shaped and triangular pores, have a certain inhibitory effect on crack propagation [21].

To gain an in-depth understanding of the microstructural evolution and micromechanical behavior of the sintered layers during TS, finite element method (FEM) and molecular dynamics (MD) have been extensively utilized. For instance, FEM analyses have been employed to examine the stress-strain behavior of sintered layers under thermal shock loading [22,23], as well as to study the influence of pore shape on crack propagation [21]. Nonetheless, these simulation models generally treat the sintering layer as a homogeneous solid or an idealized model, failing to capture its true porous structure. This approximation can severely compromise the simulation accuracy. In MD simulation, Keisuke Wakamoto et al. [24] analyzed the pore growth rates under various stress conditions (tensile, no stress, and compressive stress). Their findings indicated that the degradation behaviors of the silver sintered layer were primarily driven by crack growth and the interaction between pores and cracks under TS, while dislocation nucleation and movement were identified as the key mechanisms driving the evolution of microdefect failure. However, molecular dynamics simulations, due to their intrinsic limitations in both spatial and temporal scales, have been insufficient in capturing the macroscopic trends and distribution patterns of void evolution. As a result, the comprehensive modeling of the microstructural degradation process in sintered layers remains a critical challenge that needs to be addressed.

Despite advances through experiments and simulations, key knowledge gaps remain: (1) Lack of systematic studies on porosity evolution across entire sintered layers during TS; (2) Insufficient understanding of how microstructural evolution affects micromechanical property degradation; (3) FEM struggles to capture the complex micromechanical behavior around evolving pores.

To address these challenges, this study integrates experimental and computational approaches to systematically investigate the degradation mechanisms of silver sintered layers under TS (from −45 °C to 125 °C). Electron back scatter diffraction (EBSD) and nanoindentation are used to correlate microstructural evolution with micromechanical properties. Real microstructures from SEM are reconstructed into FEM models to simulate stress distributions around pores. The Potts model based on Kawasaki dynamics is applied to predict long-term pore evolution over large scales. By combining these methods, this work aims to clarify the degradation mechanisms of silver sintered layers during TS, providing theoretical guidance to enhance reliability and promote industrial application of pressureless sintering.

2. Materials and methods

2.1. Silver sintering process and materials

The experiment utilized the 1200V SiC die manufactured by SICHAIN, specifically the SG2M014120B model. The die dimensions were 4.8 mm × 6.3 mm × 0.2 mm. The metallization layers on the drain side consisted of a 1-μm-thick Ti/Ni/Ag stack, while the top metallization employed a 4-μm-thick Ni/Pd/Au configuration. The substrate was supplied by Ferrotec and featured a sandwich structure composed of Cu/Si_3N_4/Cu layers bonded using active metal brazing (AMB) technology. The copper layers of the AMB substrate were approximately 0.5 mm thick, and the ceramic layer was about 0.38 mm thick. To enhance the reliability of silver sintering, the top copper layer was electroplated with a 0.1–0.6 μm silver coating. The silver sintering paste used in the experiment is ALPHA ARGOMAX 2020 PASTE, provided by MacDermid Alpha (Waterbury, CT, USA).

Fig. 1(a) and (b) depict the primary sintering process flow and the equipment utilized. The sintering procedure is divided into four main stages: material preparation, silver paste printing, pre-drying, and sintering. To achieve an interconnection layer with a thickness of 20 μm, the stencil thickness is designed to be 100 μm. Printing experiments were conducted on a YAMAHA YCP10 printing machine, with the squeegee tilt angle, printing speed, and squeegee pressure set to 60°, 10 mm/s, and 0.25 N, respectively. Pre-drying experiments were performed using a Songling HYD90-2T oven equipped with an N_2 atmosphere, with the parameters set to 130 °C for 30 min. The pre-dried silver-based sintered substrates undergo hot attach process on a Datacon 2200 evo machine, with the substrate heating temperature set to 135 °C. The sintering process was carried out on a Boschman Sinterstar Innovate-F-XL system, also equipped with an N_2 atmosphere. The sintering temperature, pressure, and time were set to 250 °C, 15 MPa, and 300 s, respectively, as illustrated by the sintering profile in Fig. 1(c). The TS test was performed in a two-chamber TS test system under ambient air. The low and high temperatures were set to −45 °C and 125 °C, respectively, with a dwell time of at least 15 min at each extreme. The specific temperature profile is shown in Fig. 1(d), with parameter settings based on AQG 324 standards. Quality monitoring during the TS test was conducted using a Sonoscan water-immersion ultrasonic scanner.

2.2. Microstructure characterization

Upon completion of the experimental sample fabrication and reliability tests, cross-sectional specimens were prepared by cutting the sample perpendicular to the X-axis. The samples were ground sequentially with sandpaper of #80, #120, #400, #600, #800, #1200, and #1500 grit. Following grinding, the samples were mechanically polished using diamond suspension sprays with particle sizes of 0.5 μm and 2.5 μm. Subsequently, the polished cross-sections underwent ion milling using a standard Hitachi IM4000II ion milling instrument. To characterize the pore evolution behavior in the nano silver sintered layer during TS, the porosity distribution across the entire cross-section was quantified for samples subjected to 0 cycle and 1500 cycles. After ion milling, the sample was continuously imaged by Zeiss/GeminiSEM 360 scanning electron microscope (SEM) with an accelerating voltage of 15 kV from the left to the right side of the region beneath the die. The

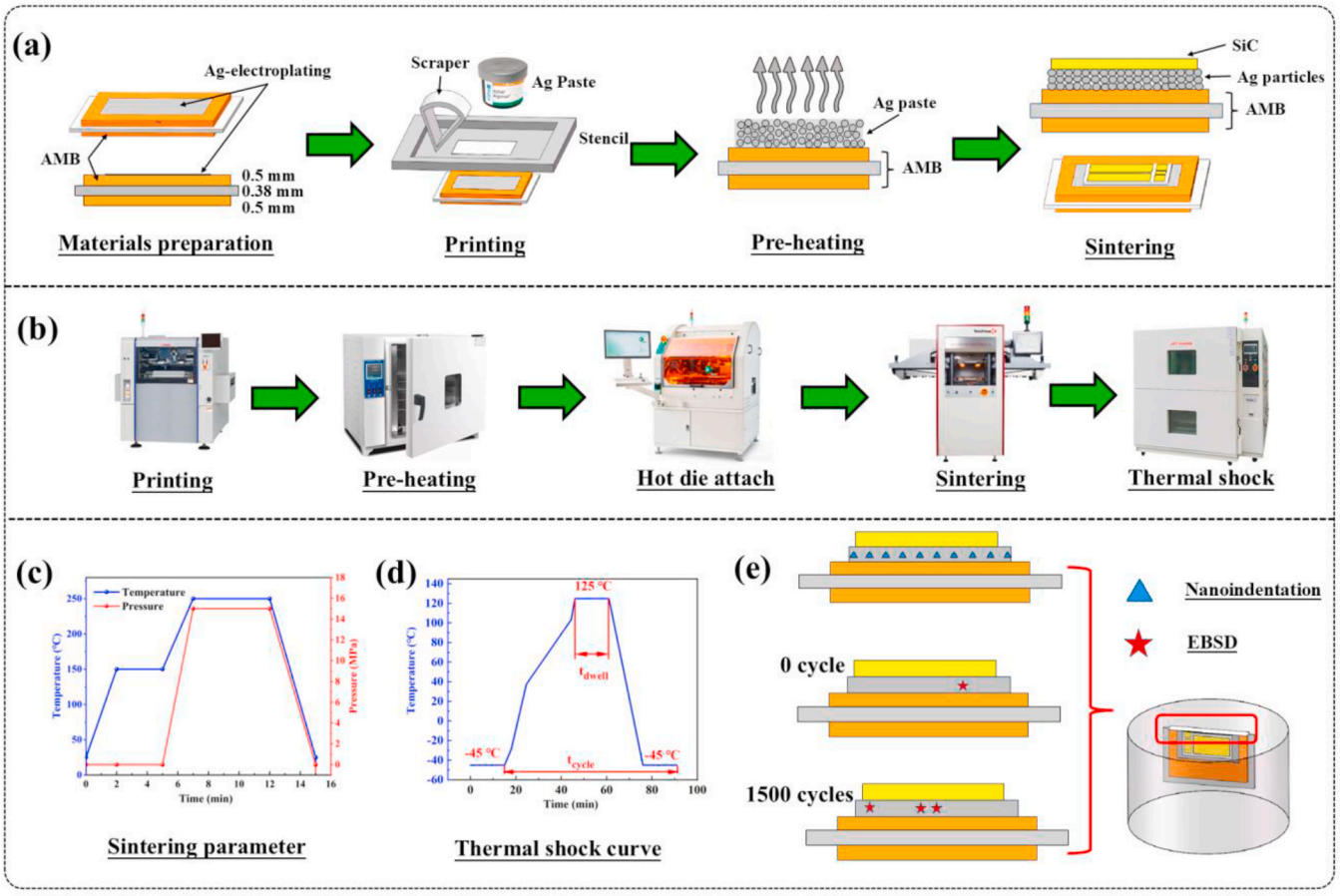


Fig. 1. Schematic illustration of: (a) sintering process, (b) test equipments, (c) sintering profile, (d) TS test profile, (e) locations of nanoindentation and EBSD characterization.

acquired images were then analyzed using Image J software to identify and quantify the porosity distribution. To investigate the microstructural evolution under different cycling conditions and its correlation with micromechanical properties, cross-sectional microstructural characterization was conducted on the Thermo Scientific Apreo 2C microscope equipped with an EDAX Velocity Super high-speed EBSD detector. The tests were performed at an accelerating voltage of 20 kV and a beam current of 6.4 nA. The EBSD scanning step size was set to 50 nm, with an image resolution of 400 × 400 pixels. To ensure precise identification of the EBSD testing areas, the relative coordinates of the regions of interest were determined using nanoindentation and optical microscopy.

The spacing between nanoindentation points was approximately 50 μm. For 0-cycle-sample, before EBSD acquisition, the target area was located based on the hardness values obtained from nanoindentation. The right edge of the die was selected as the reference line, and the measured distance between the indentation point and the chip edge was used for precise positioning. Finally, the corresponding displacement values were set on the EBSD system for imaging. For the 1500-cycle sample, distinct features can be observed in the crack area, and at the boundaries between the high-porosity region and the low-porosity region. The captured EBSD data were analyzed using TSL OIM software to determine grain size, crystal orientation, and grain boundary characteristics. Additionally, the proportions of recrystallized grains, deformed grains, and substructured grains were analyzed using HKL Channel 5 software. Quantitative analysis of geometrically necessary dislocation (GND) density was performed using MATLAB and the MTEX toolbox through custom scripts.

2.3. Micro-mechanical properties test

After ion milling, nanoindentation experiments were conducted on samples subjected to 0 cycle and 1500 cycles of TS using a KLA iNano nano-mechanical testing system equipped with a diamond Berkovich indenter. To investigate the effects of TS tests on micromechanical properties and the heterogeneity of cross-sectional micromechanical properties under 1500 cycles, nanoindentation tests were performed at cross-sectional intervals of 50 μm within the sintered layer, as shown in Fig. 1(e). The experimental parameters were set to a Target Load of 25 mN, a Target Depth of 500 nm, and a Target Indenter Strain Rate of 0.2 s^{-1}. To calculate the SSD density, nanoindentation experiments were conducted at different depths. In this case, the Target Depth was set to a range from 100 nm to 2000 nm, with the Target Load limitation configured to 50 mN. To better correlate the microstructure with micromechanical performance results, the EBSD scanning region was aligned with the nanoindentation test locations by calibrating relative distances and identifying characteristic regions. The process of converting the nanoindentation load-displacement curves into stress-strain curves was accomplished using a MATLAB-based script, which was also employed to generate graphical representations of the results.

2.4. Nanoindentation computational model

2.4.1. Hardness analysis model

Currently, nanoindentation technology has emerged as a critical tool for characterizing the micromechanical properties in the semiconductor packaging field, owing to its accuracy and convenience. The experimental results are primarily presented in the form of load-displacement

(P-H) curves. By employing the classical mechanical methodology and plastic deformation theory proposed by Oliver and Pharr, the P-H curve data can be analyzed to derive the mechanical parameters of the material under investigation, such as hardness and equivalent elastic modulus, as calculated using Eqs (1)–(4) [25,26]:

$$H = \frac{P_{\max}}{A_m} \tag{1}$$

$$E^* = \frac{S\sqrt{\pi}}{2\beta\sqrt{A_m}} \tag{2}$$

$$A_m \approx 24.56 {h_c}^2 \tag{3}$$

$$S = \left.\frac{dP}{dh}\right|_{h_m} \tag{4}$$

where H represents the hardness of the tested sample, P_{max} denotes the maximum indentation load applied to the sample, and E^* is the equivalent elastic modulus of the material. The constant β is related to the geometry of the indenter (for a diamond Berkovich indenter, $\beta = 1.034$). S is the slope of the upper portion of the unloading curve, h_c represents the contact depth, h_m is the maximum indentation depth, and A_m is the projected contact area in the vertical direction under the maximum indentation depth. The parameters P_{max} and h_m can be directly obtained from the P-h curve. The contact depth h_c can be calculated using Eq. (5) [25]:

$$h_c = h_{\max} - \varepsilon\frac{P_{\max}}{S} \tag{5}$$

where ε is a constant (for a diamond Berkovich indenter, $\varepsilon = 0.75$). In addition, E^* can also be calculated based on the elastic modulus and Poisson's ratio of the tested sample and the Berkovich indenter [26]:

$$\frac{1}{E^*} = \frac{1-\upsilon^2}{E} + \frac{1-\nu_i^2}{E_i} \tag{6}$$

where E_i and υ_i are the elastic modulus (1140 GPa) and Poisson's ratio (0.07) of the diamond Berkovich indenter, E and υ represent the elastic modulus and Poisson's ratio of the tested sample. In this study, the value of E is derived from the results of nanoindentation experiments, and the Poisson's ratio of silver is taken as 0.37 [27].

2.4.2. P-h curve transformed to stress-strain curve theory

The stress-strain curve, which aids in obtaining parameters such as material yield strength, elastic modulus, and strain hardening behavior, is a crucial indicator for evaluating the micro-mechanical properties of materials [28,29]. Nanoindentation can also be used to convert the P-H curve into a stress-strain curve through computational models. It is well-known that the yield strength marks the boundary between elastic and plastic deformation. The elastic deformation stage can be represented by a linear region based on yield strength and elastic modulus, while the plastic deformation phase can be calculated using Eq. (7) [27]:

$$\sigma = \begin{cases} E\varepsilon & \sigma \le \sigma_y \\ \sigma_y\left(1 + \dfrac{E}{\sigma_y}\varepsilon_p\right)^n & \sigma > \sigma_y \end{cases} \tag{7}$$

where ε is the elastic strain, n is the strain hardening exponent, σ_y is yield strength, and ε_p is plastic strain. Therefore, to plot the stress-strain curve, it is necessary to calculate the parameters n and σ_y.

The maximum indentation area can be calculated using Eq. (8) [30]:

$$\frac{1}{E^*\sqrt{A_m}}\left.\frac{dP_m}{dh}\right|_{h_m} = c^* \tag{8}$$

where c^* is taken as 1.167 for the diamond Berkovich, and E^* can be calculated by Eq. (6). Based on previous studies, it is known that the P-H curve during the loading stage can be fitted to a quadratic function to obtain the quadratic coefficient C. Subsequently, C and E^* are substituted into Eq. (9), and $\sigma_{0.033}$ is obtained through Newton's iteration method. $\sigma_{0.033}$ is considered a normalized dimensionless function and is related to the strain hardening exponent [30].

$$\frac{C}{\sigma_{0.033}} = \prod_1\left(\frac{E^*}{\sigma_{0.033}}\right) = -1.131\left[\ln\left(\frac{E^*}{\sigma_{0.033}}\right)\right]^3 + 13.635\left[\ln\left(\frac{E^*}{\sigma_{0.033}}\right)\right]^2 - 30.594\left[\ln\left(\frac{E^*}{\sigma_{0.033}}\right)\right] + 29.267 \tag{9}$$

where Π_1 is a dimensionless function. Then, by substituting $\sigma_{0.033}$ into Eq. (10) and applying the Newton-Raphson method, the strain hardening exponent n can be obtained [30]:

$$c^* = \prod_2\left(\frac{E^*}{\sigma_{0.033}}, n\right) = \left(-1.4n^3 + 0.78n^2 + 0.16n - 0.068\right)\left[\ln\left(\frac{E^*}{\sigma_{0.033}}\right)\right]^3 + \left(17.93n^3 - 9.22n^2 - 2.38n + 0.863\right)\left[\ln\left(\frac{E^*}{\sigma_{0.033}}\right)\right]^2 + \left(-80n^3 + 40.56n^2 + 9n - 2.545\right)\left[\ln\left(\frac{E^*}{\sigma_{0.033}}\right)\right] + \left(122.65n^3 - 63.9n^2 - 9.59n + 6.2\right) \tag{10}$$

where Π_2 is a dimensionless function. The yield strength σ_y can then be calculated by substituting $\sigma_{0.033}$ and n into Eq. (11) [30]:

$$\sigma_{0.033} = \sigma_y\left(1 + \frac{E}{\sigma_y} \times 0.033\right)^n \tag{11}$$

Finally, the calculated parameters, σ_y, and n, are substituted into Eq. (7) to obtain the stress-strain curve.

2.4.3. SSD calculation theory

Dislocation strengthening is an essential mechanism that cannot be overlooked in metal materials. In nanoindentation experiments, hardness typically decreases with increasing indentation depth, a phenomenon known as the indentation size effect (ISE) [31]. Nix and Gao [31] have demonstrated that the ISE is often associated with the GND density. As the indentation depth and deformation increase, GND density changes to accommodate the strain gradient beneath the indentation. However, SSD density does not exhibit a dependence on indentation size. Consequently, nanoindentation serves as an effective method for characterizing SSD.

The equivalent flow stress σ can be transformed into hardness H by Eqs. (12) and (13) [31,32]:

$$\sigma = \sqrt{3}\tau \tag{12}$$

$$H = 3\sigma \tag{13}$$

where the value of 3 represents Tabor's factor, τ denotes the shear strength. The shear strength can be calculated using Eq. (14) [31,32]:

$$\tau = \alpha G b\sqrt{\rho_T} \tag{14}$$

where ρ_T is the total dislocation density, comprising both GND and SSD. G denotes the shear modulus (taken as 26.4 GPa in this study), b is the Burgers vector (0.286), α is a constant (0.5). The size effect in nanoindentation can be described using Eqs. (15) and (16) [31,32]:

$$H_0 = 3\sqrt{3}\alpha G b\sqrt{\rho_{SSD}} \tag{15}$$

$$H = 3\sqrt{3}\alpha G b\sqrt{\rho_{SSD} + \rho_{GND}} \tag{16}$$

where H_0 represents the hardness derived from SSD density, and H denotes the hardness at a specific indentation depth. The relationship between H_0 and H can be expressed by Eq. (17) [31]:

$$H \Big/ H_0 = \sqrt{1 + \frac{h^*}{h}} \tag{17}$$

where the ratio of ρ_{GND} and ρ_{SSD} can be expressed as:

$$\frac{\rho_{GND}}{\rho_{SSD}} = \frac{h^*_{GB}}{hf^3} = \frac{h^*}{h} \tag{18}$$

where h^* can be expressed as:

$$h^* = \frac{81}{2} b\alpha^2 \tan^2\theta \left(\frac{G}{H_0}\right)^2 \tag{19}$$

where h^*_{GB} refers to the characteristic scale of the GND density and h, f is a corrected material constant that accounts for the precise volume including GND. h^* refers to the characteristic length determined by SSD density [33]. Ultimately, Eq. (17) can be expressed as [31,32]:

$$H \Big/ H_0 = \sqrt{1 + \frac{h^*}{h}} \tag{20}$$

During the experiment, the depth of the indentation can be adjusted to plot and fit $H^2 - 1/h$, where the y-intercept of the linear fit represents H_0^2 [27,32,34]. Finally, the SSD density can be calculated by Eq. (15).

In summary, nanoindentation is an effective method for characterizing the micromechanical properties of SiC die attach layers, including hardness, yield strength, and SSD density.

3. Results

3.1. Microstructure characteristics

3.1.1. Pore evolution during TS

Fig. 2 shows the cross-sectional SEM images of the sintered layer before and after 1500 cycles TS test with porosity distribution and overall morphology evolution, where the blue and red curves represent the overall porosity distribution of the cross-section at 0 cycle and 1500 cycles, respectively. It can be observed that at 0 cycle, the porosity distribution across the cross-section is relatively uniform, with an average porosity of approximately 9.97 % ± 1.74 %. Fig. 2(A1) and (A2) represent the highest and lowest porosities of the cross-section, which are approximately 12.93 % and 6.15 %, respectively. However, after 1500 cycles, the porosity in the cross-section shows a pronounced heterogeneous distribution. Fig. 2(B1) and (B2) show that the highest and lowest porosities are 22.12 % and 5.61 %, respectively, with the bottom of (B2) beginning to show a trend of pores merging into cracks. Moreover, the individual pore size is essentially larger than the 0-cycle pore size, with a reduced number of pores. The distribution curves also reveal a significant pattern: areas with higher porosity are often accompanied by adjacent areas with lower porosity, with the average porosity remaining 10 %. However, previous research [24] suggested that under the effect of TS, pores tend to expand at their initial locations. For further study, this paper statistically analyzes the porosity of the entire sintered layer after 1500 cycles. The statistical results show that the average porosity of the entire cross-section after 1500 cycles is still 10.16 % ± 4.69 %, which is almost identical to the average porosity of the 0 cycle (9.97 % ± 1.74 %). It indicates that under the effect of TS, the pores in the silver sintered layer do not expand or shrink at their initial locations but undergo diffusion and aggregation, resulting in the appearance of low porosity areas surrounding high porosity areas after 1500 cycles. Additionally, cracks caused by pore aggregation are observed at the die edges and near the die edges, as shown in Fig. 2(B3) and (B4). Statistical analysis shows that the porosity in B3 is approximately 10.85 %, while the porosity in B4 reaches 23.06 %. After 1500

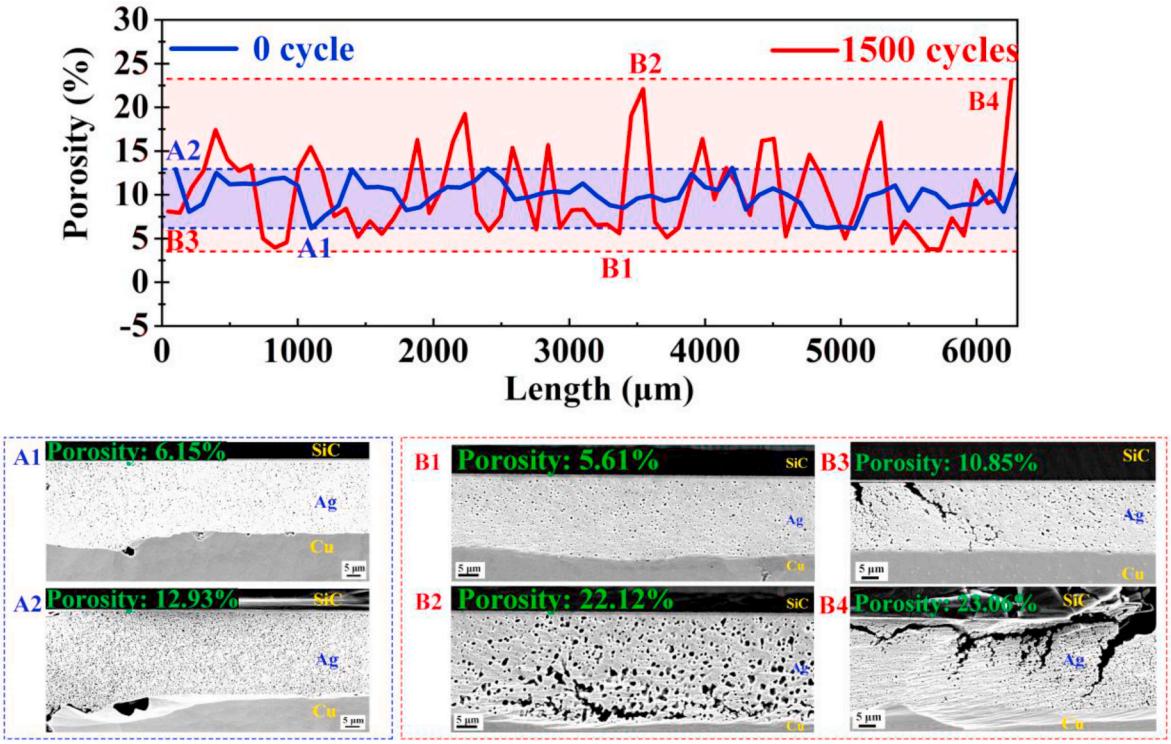


Fig. 2. Cross-sectional SEM images of the sintered layer before and after 1500 cycles TS test with porosity distribution and overall morphology evolution.

cycles, the crack propagation within the sintered layer is relatively limited, while cracks at the edges of the sintered layer show significant expansion and merging toward the interior of the sintered layer.

In summary, under TS, the porosity in the sintered layer undergoes migration, aggregation, and merging, while the average porosity remains nearly unchanged. It is consistent with previous observations obtained using localized three-dimensional pore structure models [35]. The initiation and propagation of cracks near the die edges are significantly easier than those in the interior of the sintered layer.

3.1.2. *Microstructure features evolution during TS*

Fig. 3 shows the inverse pole figures (IPFs), orientation distribution functions (ODFs), and corresponding statistical analysis of grain size distribution of the sintered layer before and after 1500 cycles (crack region, high-porosity area, and low-porosity area at 1500 cycles). Fig. 3 (a) and (i) show the IPFs and grain size distribution of the sintered layer at 0 cycle. It can be observed that the die-attach layer exhibits a fine and uniformly distributed equiaxed grain structure after the sintering, with no significant preferred orientation. Statistical analysis reveals that the grain size distribution follows a Gaussian model, with a high R-squared value of 0.963, and an average grain size of approximately 0.377 μm ± 0.14 μm, larger than the particles size before sintering (pre-sintering silver powder particles measured approximately 0.292 μm ± 0.032 μm [33]). Fig. 3 (e) shows the ODFs at 0 cycle, where it can be observed that the die attach, subjected to the compressive force of the mold during the sintering process, forms rolling textures of Rotated Brass and Copper, with a texture strength of approximately 1.521 multiples of random distribution (MRD). Fig. 3 (b) and (j) show the IPFs and grain size distribution in the crack region at 1500 cycles. It is evident that in the crack region, equiaxed grains experience slight deformation and significant growth, resulting in an uneven grain size distribution. The grain size distribution, while still approximating a Gaussian distribution, shows a decrease in the R-squared value to 0.89, likely due to the differences in grain growth rates. Moreover, the grain size has significantly increased to 1.05 μm ± 0.49 μm, representing a 2.8-fold growth compared to the 0 cycle. It suggests that the cyclic load under high and low temperatures serves as a driving force, significantly promoting grain growth. Fig. 3(f) shows the ODFs of the sintered layer in the crack region after 1500 cycles. It is evident that the texture of the sintered layer evolves into recrystallized textures consisting of $Cube_{ND}$, $Cube_{RD}$, shear textures B/$\overline{B}$ and A, while retaining the initial rolled textures, including Rotated Brass and Copper. The texture strength increases to 2.085 MRD. In the high-porosity region after 1500 cycles, the grain size is approximately 0.79 ± 0.36 μm, which is about 25 % smaller than that in the crack region, as shown in Fig. 3(c) and (k). However, the grain size is still approximately 2.1 times larger compared to the 0-cycle die attach. Fig. 3 (g) shows the ODFs of the high-porosity region. It can be observed that the high-porosity region primarily evolves into the Goss texture, with a texture strength of 2.018 MRD. Fig. 3(d) and (l) display the IPF and grain size statistics of the low-porosity region after 1500 cycles. The grain size in this region is approximately 0.83 μm ± 0.34 μm, which is a 2.2-fold increase compared to the 0-cycle region. It is noting that the grain size in the low-porosity region is still smaller than that in the crack region. As shown in Fig. 3(h), the texture of the low-porosity region is predominantly composed of Rotate Goss and B/$\overline{B}$ textures, with a texture strength of approximately 1.949 MRD.

In conclusion, under TS, the grain size and texture intensity of the die

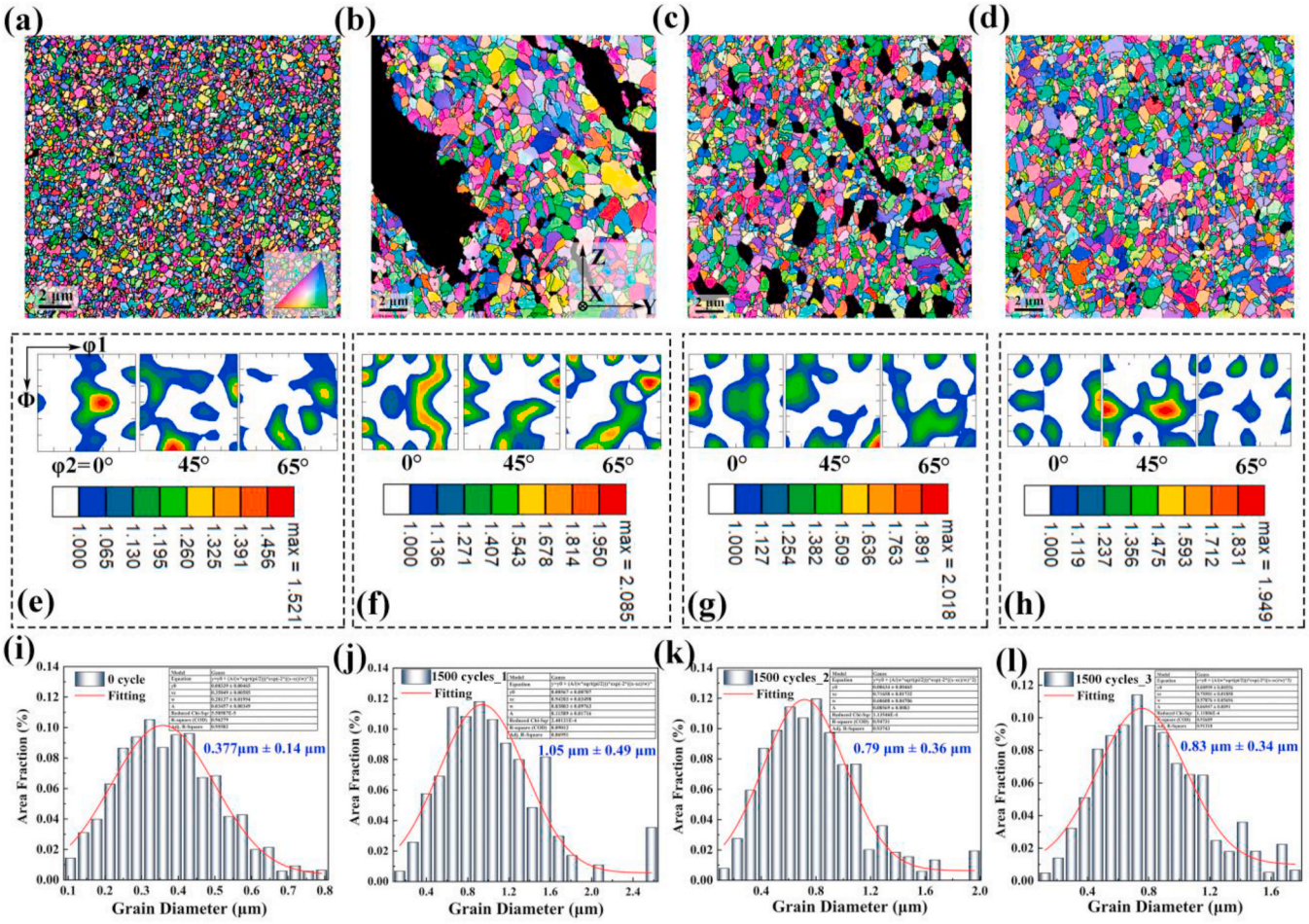


Fig. 3. (a)–(d) IPFs, (e)–(h) ODFs, and (i)–(l) corresponding statistical analysis of grain size distribution of the sintered layer before and after 1500 cycles TS test.

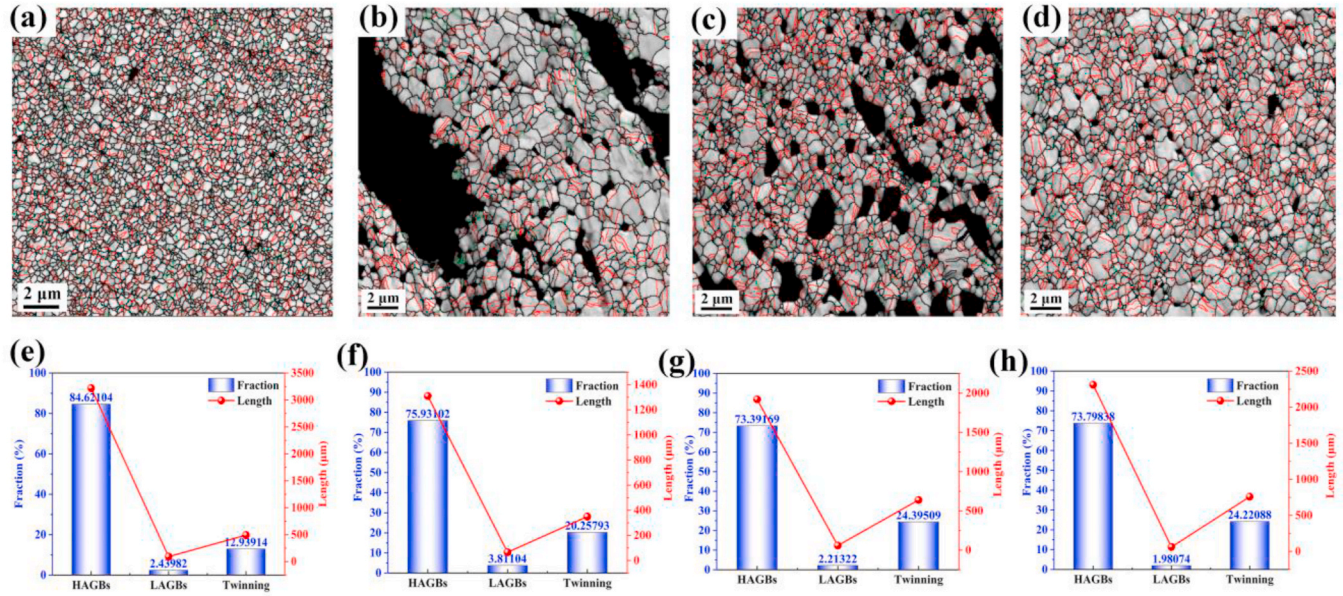


Fig. 4. (a)–(d) Grain boundaries distribution maps and (e)–(h) corresponding statistical analysis of the sintered layer before and after 1500 cycles TS test.

attach significantly increase, with respective increases of approximately 110 %–179 % and 28 %–37 %. The most substantial increases were observed in the crack regions.

Fig. 4 shows the grain boundary distribution and corresponding statistical analysis of the sintering layer before and after 1500 cycles (crack region, high porosity region, and low porosity region at 1500 cycles). In the figure, black solid lines represent high-angle grain boundaries (HAGBs, misorientation angle >15°), green solid lines represent low-angle grain boundaries (LAGBs, misorientation angle between 2° and 15°), and red lines indicate two types of recrystallization twins (with axis-angle values of approximately 60° and 38.9°). According to Fig. 4(a) and (e), at 0 cycle, the lengths of HAGBs and LAGBs are approximately 3220 μm and 92.84 μm, respectively, accounting for 84.6 % and 2.4 % of the total grain boundary length. The total length of the two recrystallization twin boundaries is approximately 492 μm, representing around 13 % of the total grain boundary length. Fig. 4(b) and (f) depict the grain boundary distribution and statistical data in the crack region at 1500 cycles. It is observed that the lengths of HAGBs and LAGBs in the crack region are approximately 1310 μm and 65.75 μm, accounting for 75.9 % and 3.8 % of the total grain boundary length,

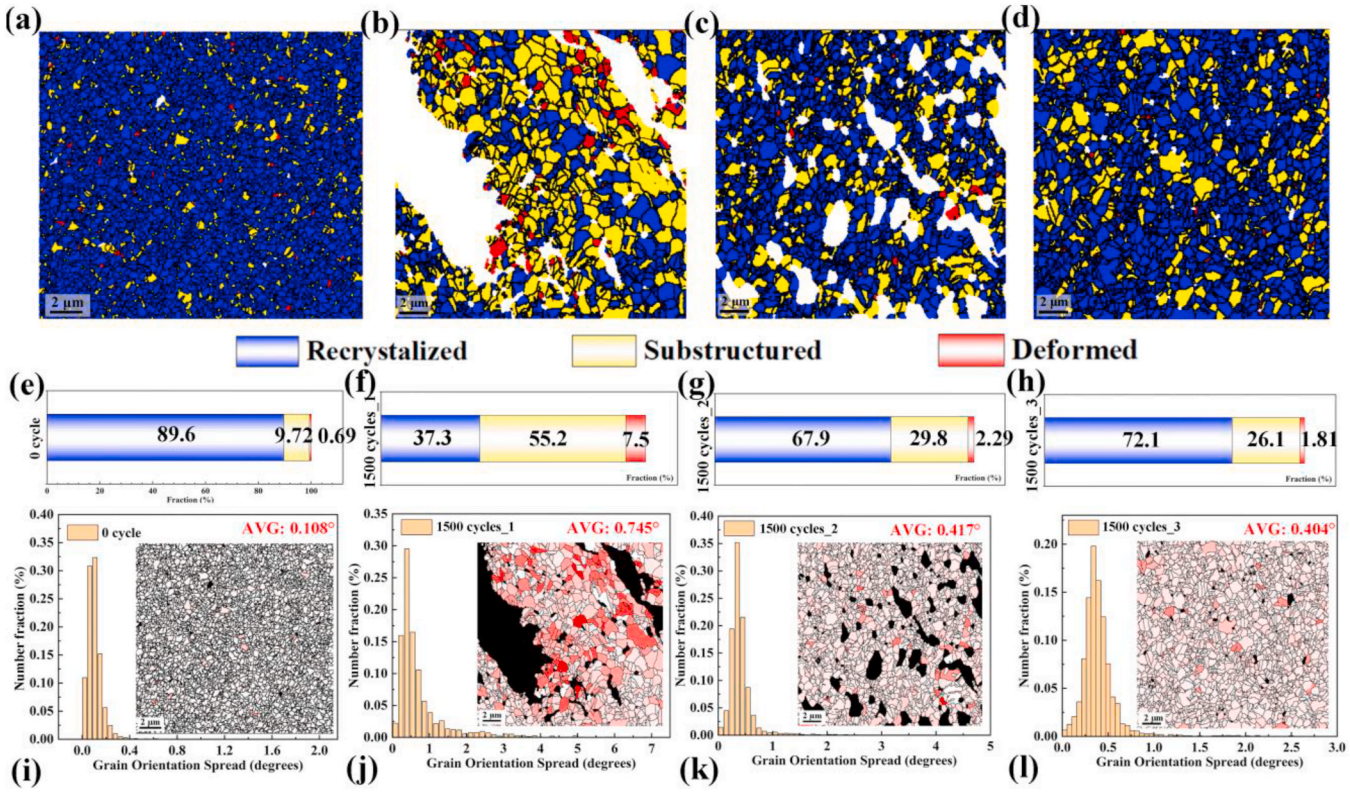


Fig. 5. (a)–(d) RF distribution, (e)–(h) RF histograms, and (i)–(l) statistical GOS distributions in the sintered layer before and after 1500 cycles TST test.

respectively. The total length of the two recrystallization twins is 349.5 μm, making up 20.3 % of the total grain boundary length. Fig. 4(c) and (g) show the grain boundary distribution and statistical data for the high porosity region at 1500 cycles. The lengths of HAGBs and LAGBs are 1920 μm and 57.9 μm, which account for 73.4 % and 2.2 % of the total grain boundary length, respectively. The twin boundary length is 638.2 μm, representing 24.4 % of the total grain boundary length. For the low porosity region at 1500 cycles, the lengths of HAGBs, LAGBs, and twin boundaries are 2310 μm, 62 μm, and 758.15 μm, respectively, accounting for 73.8 %, 2.0 %, and 24.2 % of the total grain boundary length. It can be inferred that the significant grain growth under TS led to a reduction of approximately 10 %–13 % in the HAGBs, while the twin boundaries increased by approximately 57 %–89 %. However, the change in LAGBs is minimal. Furthermore, at 1500 cycles, the proportion of twin boundaries in the crack region is lower than in other regions, indicating that the process of pore merging into cracks is accompanied by the disappearance of twin boundaries.

Fig. 5 shows the recrystallization fraction (RF) and statistical Grain Orientation Spread (GOS) before and after 1500 cycles (crack zone, high porosity region, and low porosity region at 1500 cycles), where blue grains represent recrystallized grains, yellow grains represent substructured grains, and red grains represent deformed grains. The white-to-red color in the GOS distribution represents a gradual increase in grain misorientation degrees. Fig. 5(a), (e) and (i) show the recrystallized grain distribution, histograms, and statistical GOS distribution at 0 cycle, respectively, where the recrystallization distribution at 0 cycle refers to the transformation of nano-silver particles—from their initial powder particles—into a recrystallized porous microstructure under the combined effects of temperature and pressure during sintering. It can be observed that the silver sintered layer is formed through diffusion and recrystallization, with the proportion of recrystallized grains reaching 89.6 %, while substructure and deformed grains account for 9.72 % and 0.69 %, respectively. Due to the high RF at 0 cycle, the average misorientation angle is small, approximately 0.108°. However, at 1500 cycles, the proportion of recrystallized grains in the crack zone significantly decreases to only 37.3 %, while substructured and deformed grains increase to 55.2 % and 7.5 %, as shown in Fig. 5(b) and (f). Additionally, the average misorientation angle significantly increases to 0.745°, which is 6.9 times higher than the 0 cycle, as shown in Fig. 5(j). According to Fig. 5(c), (d), (g), and (h), in the high porosity and low porosity regions at 1500 cycles, the proportion of recrystallized grains decreases only slightly, accounting for 67.9 % and 72.1 %, respectively. The substructured grains increase to 29.8 % and 26.1 %, while deformed grains account for 2.29 % and 1.81 %, respectively. Furthermore, in the high and low porosity regions at 1500 cycles (Fig. 5(k) and (l)), the average misorientation angle is approximately 0.417° and 0.404°, respectively. It suggests that under TS, recrystallized grains gradually transform into substructured and deformed grains. Moreover, based on the comparison between the low-porosity region and the crack zone, it can be observed that as the pores merge and cracks form, the proportion of recrystallized grains transforming into substructured and deformed grains increases, and the average misorientation angle also shows a gradual increase. It suggests that the mismatch of CTE induces a stress concentration in the die attach. Once achieving a critical value, the slip

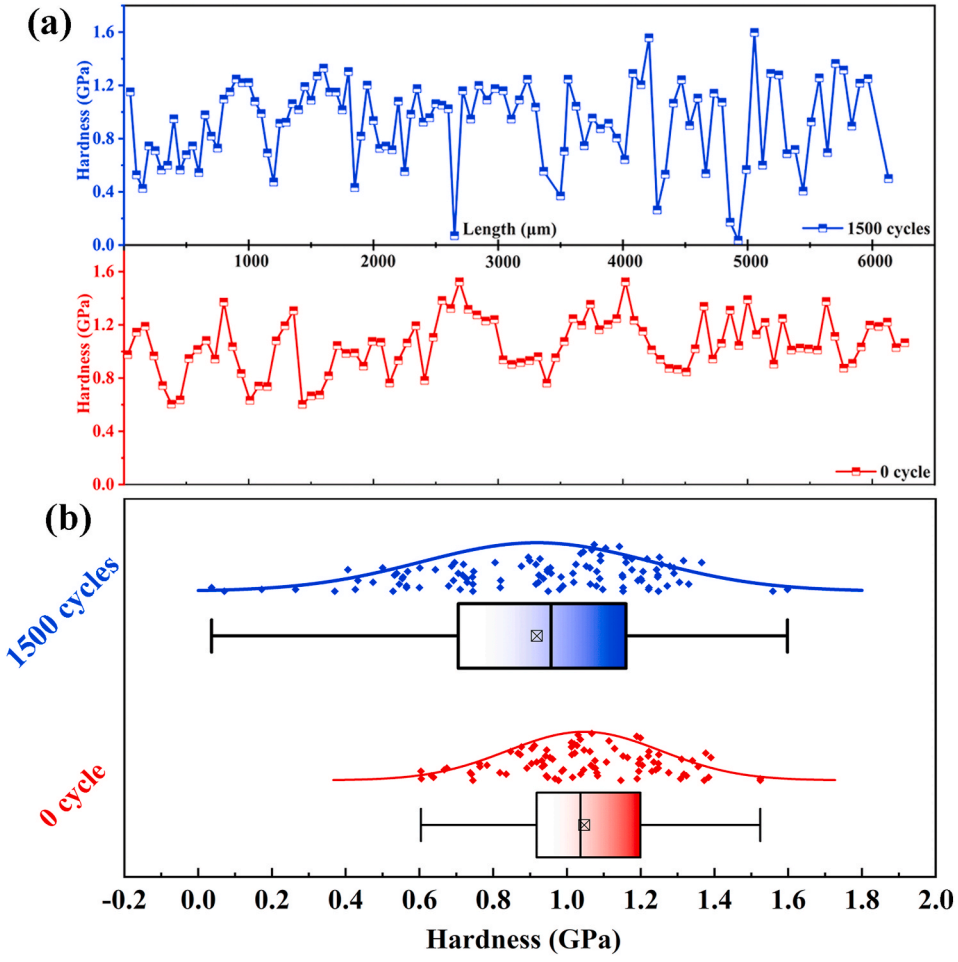


Fig. 6. Comparison of nanoindentation hardness distribution of sintered layer before and after 1500 cycles TS test: (a) hardness distribution along the cross-section, (b) statistical hardness distribution.

system inside the grain is activated, leading to the creation and increase of dislocations, which in turn causes an increase in misorientation.

In conclusion, under the TS, the proportion of recrystallized grains significantly decreases, transforming into substructured and deformed grains, accompanied by a marked increase in the average misorientation angle.

3.2. Micro-mechanical properties

3.2.1. Hardness distribution and evolution

To investigate the effect of TS on the micromechanical performance evolution of SiC die sintered layers, nanoindentation tests were conducted at intervals of 50 μm along the length, with the results presented in Fig. 6. Fig. 6(a) illustrates the comparison of nanoindentation hardness distribution along the the cross-section before and after 1500 cycles

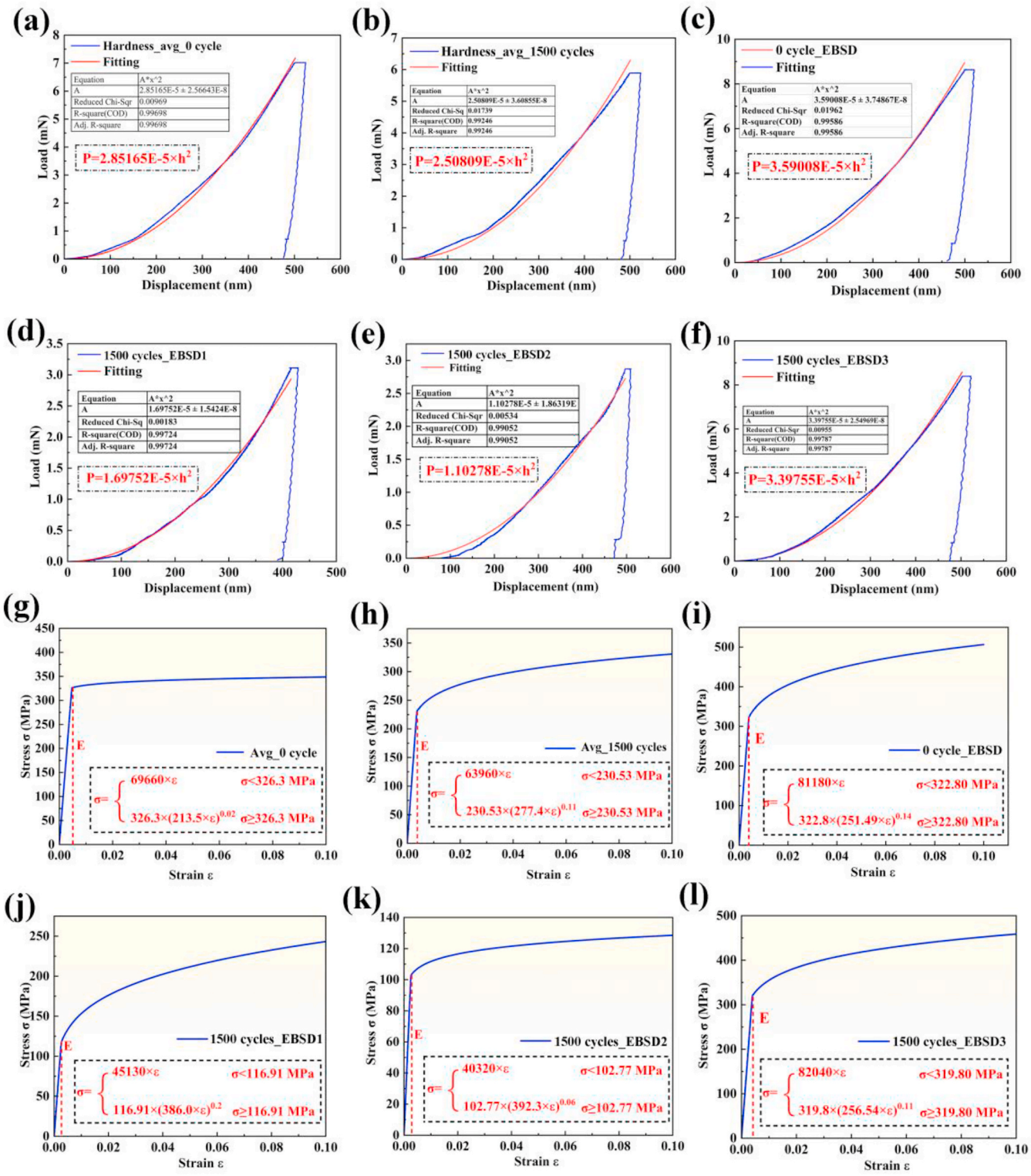


Fig. 7. (a)–(f) Load-displacement curves and (g)–(l) corresponding stress-strain curves of the sintered layer before and after 1500 cycles TS test.

TS test, where the blue line represents the hardness distribution after 1500 cycles and the red line corresponds to the 0 cycle. The nano-indentation hardness of the sintering layer under 0 cycles is generally distributed around 1.05 GPa ±0.21 GPa, with maximum and minimum hardness values of approximately 1.6 GPa and 0.6 GPa, respectively. The hardness distribution exhibits good consistency. However, after 1500 cycles, the overall hardness of the sintered layer decreases, with an average hardness of approximately 0.92 GPa ±0.31 GPa, representing a reduction of about 12.4 % compared to the 0 cycle. Furthermore, the maximum hardness decreases slightly to ~1.56 GPa, while the minimum hardness approaches 0 GPa. The significant decrease in hardness is primarily attributed to the loose structures in regions with high porosity and cracks, which fail to support the load exerted by the indenter. Fig. 6 (b) shows the statistical distribution of hardness for 0 cycle and 1500 cycles. Based on statistical analysis, the hardness of the sintered layer under the 0-cycle condition is mainly distributed between 0.9 and 1.2 GPa. In contrast, under the 1500-cycle condition, the hardness is distributed between 0.7 and 1.2 GPa. The standard deviations for the 0-cycle and 1500-cycle conditions are 0.21 GPa and 0.31 GPa, respectively, indicating a more dispersed hardness distribution after 1500 cycles. Furthermore, the median hardness values for the 0-cycle and 1500-cycle conditions are 1.04 GPa and 0.96 GPa, respectively, demonstrating a significant decrease in the hardness of the sintered layer after high- and low-thermal shock test.

3.2.2. Nanoindentation stress-strain curve

Fig. 7 illustrates the load-displacement curves and the corresponding stress-strain curves calculated according to 2.4.2 before and after 1500 cycles TS test. Specifically, Avg_0 cycle and Avg_1500 cycles represent the P-H curves and stress-strain curves for the average hardness of the sintered layer at 0 cycle and 1500 cycles, respectively. Furthermore, 0 cycle_EBSD, 1500 cycles_EBSD1, 1500 cycles_EBSD2, and 1500 cycles_EBSD3 correspond to the hardness obtained from EBSD regions at 0 cycle, the crack region, the high-porosity region, and the low-porosity region at 1500 cycles, respectively. As shown in Fig. 7(a)–(f), the R-square values of the P-H curves during the loading stage all exceed 0.99, indicating excellent fitting accuracy and reliable fitting parameters. The quadratic coefficients are summarized in Table 1. Based on the fitting results, the stress-strain functions are derived and presented in Eqs (21)–(26):

Avg_0 cycle:

$$\sigma = \begin{cases} 69660 \times \varepsilon & \sigma \le 326.3MPa \\ 326.3 \times (213.5 \times \varepsilon)^{0.02} & \sigma > 326.3MPa \end{cases} \quad (21)$$

Avg_1500 cycles:

$$\sigma = \begin{cases} 63960 \times \varepsilon & \sigma \le 230.53MPa \\ 230.53 \times (277.4 \times \varepsilon)^{0.11} & \sigma > 230.53MPa \end{cases} \quad (22)$$

0 cycle_EBSD:

$$\sigma = \begin{cases} 81180 \times \varepsilon & \sigma \le 322.80MPa \\ 322.80 \times (251.5 \times \varepsilon)^{0.14} & \sigma > 322.80MPa \end{cases} \quad (23)$$

1500 cycles_EBSD1:

$$\sigma = \begin{cases} 45130 \times \varepsilon & \sigma \le 116.91MPa \\ 116.91 \times (386.0 \times \varepsilon)^{0.2} & \sigma > 116.91MPa \end{cases} \quad (24)$$

1500 cycles_EBSD2:

$$\sigma = \begin{cases} 40320 \times \varepsilon & \sigma \le 102.77MPa \\ 102.77 \times (392.3 \times \varepsilon)^{0.06} & \sigma > 102.77MPa \end{cases} \quad (25)$$

1500 cycles_EBSD3:

$$\sigma = \begin{cases} 82040 \times \varepsilon & \sigma \le 319.80MPa \\ 319.80 \times (256.5 \times \varepsilon)^{0.11} & \sigma > 319.80MPa \end{cases} \quad (26)$$

Based on the computational results, the average yield strength of the silver sintered layer under 0 cycle is approximately 326.3 MPa. The yield strength of the sintered layer under 0 cycle (measured in the EBSD observation area) is approximately 322.80 MPa. After 1500 cycles, the average yield strength of the sintered layer decreases to 230.53 MPa, representing a reduction of about 29 % compared to the 0-cycle condition. Additionally, under 1500 cycles, the yield strengths in the crack zone, high-porosity zone, and low-porosity zone of the sintered layer observed via EBSD are calculated to be approximately 116.91 MPa, 102.77 MPa, and 319.80 MPa, respectively. It indicates that the sintered layer exhibits different degrees of strength degradation after TS, with regions of higher porosity experiencing more significant reductions in strength, where the crack zone shows the lowest yield strength. Furthermore, the ratio of hardness to yield strength was calculated to be approximately 2.9–3.9, which aligns well with Tabor's empirical values [36]. This finding suggests that the Tabor relationship is also applicable for approximating the correlation between hardness and yield strength in sintered layers.

In summary, the sintered layer showed a significant yield strength reduction under TS, where the higher porosity region is often accompanied by a more severe mechanical property degradation.

4. Discussion

4.1. The relationship between mechanical properties degradation and microstructure evolution

The strengthening behavior of metal materials is primarily governed by four mechanisms: precipitation strengthening, dislocation strengthening, grain refinement strengthening, and solid solution strengthening [37]. In the nano-silver sintered layer of SiC dies, the absence of solute atoms renders solid solution strengthening negligible in its contribution to the mechanical properties. Additionally, the nano-silver sintered layer is a precipitation-free metal layer, making the effect of precipitation strengthening on its mechanical performance insignificant. Therefore, grain refinement strengthening and dislocation strengthening are the dominant factors influencing the mechanical properties of the sintered layer.

4.1.1. Influence of grain features on degradation behaviors

A reduction in grain size corresponds to an increase in the number of grain boundaries, which often impede the movement of dislocations. The Hall-Petch relationship serves as a critical link between grain size and yield strength. The yield strength increment caused by grain size can

Table 1
Summary of parameters for the transformation of P-h curves into stress-strain curves.

	C (GPa)	H (GPa)	E (GPa)	E^*(GPa)	A_m (nm^2)	dP_{max}/dh (N/m)	$\sigma_{0.033}$ (GPa)	n	σ_y (GPa)
Avg_0 cycle	28.52	1.046	69.66	75.4	8.17E-12	266583	0.3414	0.022	0.3263
Avg_1500cycles	25.08	0.916	63.96	69.6	7.32E-12	232971	0.2965	0.109	0.2305
0 cycle_EBSD	35.90	1.324	81.18	86.92	6.79E-12	280151	0.4408	0.140	0.3228
1500cycles_EBSD1	16.98	0.426	45.13	50.0	4.51E-12	131310	0.1978	0.201	0.1169
1500cycles_EBSD2	11.03	0.406	40.32	44.9	7.95E-12	156515	0.1207	0.061	0.1028
1500cycles_EBSD3	33.98	1.247	82.04	86.92	7.13E-12	287159	0.4105	0.112	0.3198

be calculated using the Hall-Petch relationship, as expressed in Eq. (27) [38]:

$$\Delta\sigma_{H-P} = \frac{K_y}{\sqrt{D}} \tag{27}$$

where $\Delta\sigma_{H-P}$ is the yield strength increment caused by grain refinement strengthening, D is the grain size, K_y is the Hall-Petch coefficient (a constant that depends on materials properties). In different grain size ranges, the value of K_y often varies. Based on the aforementioned grain size statistical results, the grain sizes for the 0-cycle region, the crack region, the high-porosity region, and the low-porosity region after 1500 cycles are 0.377 μm, 1.05 μm, 0.79 μm, and 0.83 μm, respectively. The K_y value can be determined using Eq. (28) [39]:

$$K_y = M\left[\frac{\pi M^* G b \tau_c (2-\nu)}{4(1-\nu)}\right]^{\frac{1}{2}} \tag{28}$$

where M is Taylor factor (3.06 in FCC metals) [39], M^* is the Sachs orientation factor (2.2), α_p takes the value of 1, τ_c = 15–31 MPa.

Based on the calculation results, the value of K_y is determined to be 0.085 MPa $\sqrt{m}$. Consequently, by combining the results from Eqs. (27) and (28), the yield strength increments in the 0-cycle region, the crack region, the high-porosity region, and the low-porosity region after 1500 cycles are approximately 139 MPa, 83 MPa, 96 MPa, and 95 MPa, respectively. It indicates that due to the mismatch in CTE, the sintered layer is subjected to cyclic tensile and compressive stresses along the Y-direction when exposed to high and low-thermal shocks. The cyclic thermal stress results in significant grain growth. Furthermore, the differential grain growth caused by pore evolution leads to distinct degradation in micromechanical properties. Compared to the sintered layer in the 0-cycle region, the yield strength of the sintered layer after 1500 cycles decreases by approximately 40 % in the crack region, 31 % in the high-porosity region, and 32 % in the low-porosity region. Therefore, regions where pores accumulate and coalesce into cracks tend to exhibit larger grain sizes. Furthermore, under TS, the growth of grain size directly contributes to the decline in yield strength and hardness.

4.1.2. Influence of dislocation density on degradation behaviors

Fig. 8 illustrates the GNDs distribution and corresponding statistical analysis of the sintered layer before and after 1500 cycles TS test. Fig. 8 (a) and (e) show the GNDs distribution and statistical results for the sintered layers at 0 cycle. It can be observed that before undergoing reliability testing, the sintered layers exhibit relatively low GND densities. The dislocation density distribution follows a Gaussian profile, with an average value of approximately 2.08 × 10^{14} m^{-2} and a mode of approximately 1.74 × 10^{14} m^{-2}. However, after 1500 thermal cycles, a significant increase in GNDs density is observed. As shown in Fig. 8(d) and (h), even in the low-porosity areas after 1500 cycles, the GNDs density demonstrates a notable increase, with the average density rising to 4.66 × 10^{14} m^{-2}, which is approximately 2.2 times higher than the value at 0-cycle region. In the high-porosity areas after 1500 cycles, the GNDs density increases even more substantially, reaching approximately 5.05 × 10^{14} m^{-2}, representing a 2.4-fold increase compared to the 0-cycle value, as shown in Fig. 8(c) and (g). Furthermore, in the crack regions after 1500 cycles, an exceptionally pronounced rise in GNDs density is evident. Statistical analysis reveals that the GNDs density reaches 9.43 × 10^{14} m^{-2}, approximately 4.5 times higher than the value at 0 cycle, as illustrated in Fig. 8(b) and (f). Additionally, it also reveals that higher GNDs densities are typically concentrated around the pores. Combined with micromechanical properties, the area exhibiting more severe degradation in mechanical performance, such as the crack and high-porosity areas, corresponds to higher GNDs densities. Previous MD studies have demonstrated that dislocation nucleation and movement are the primary mechanisms driving the evolution of micro-pores [21]. From the observed data, the widespread increase in GNDs density across the sintered layers after 1500 cycles, as well as the dislocation accumulation in crack regions, suggests that TS provides the driving force for dislocation generation and motion, which promotes pore migration and coalescence.

Fig. 9 shows the representative nanoindentation *P-H* curves and the corresponding linear fitting plots of H^2-$1/h$ at different depths of the sintered layer under TS test. The linear fitting R-Square values for the four regions are approximately 0.999, 0.985, 0.942, and 0.999, respectively, indicating high reliability of the linear fitting data. Based on the *y*-intercepts of the fitted curves, the H_0 (caused by SSDs densities)

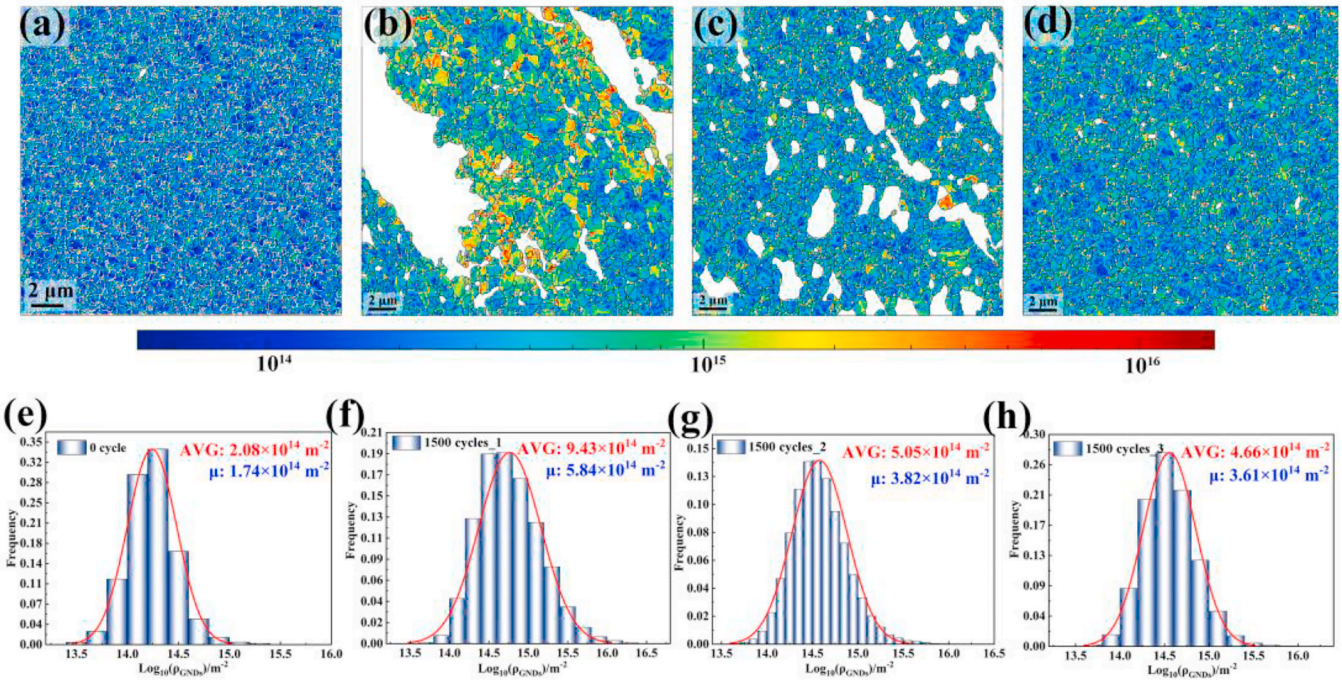


Fig. 8. (a)–(d) GNDs distribution and (e)–(h) corresponding statistical analysis of the sintered layer before and after 1500 cycles TS test.

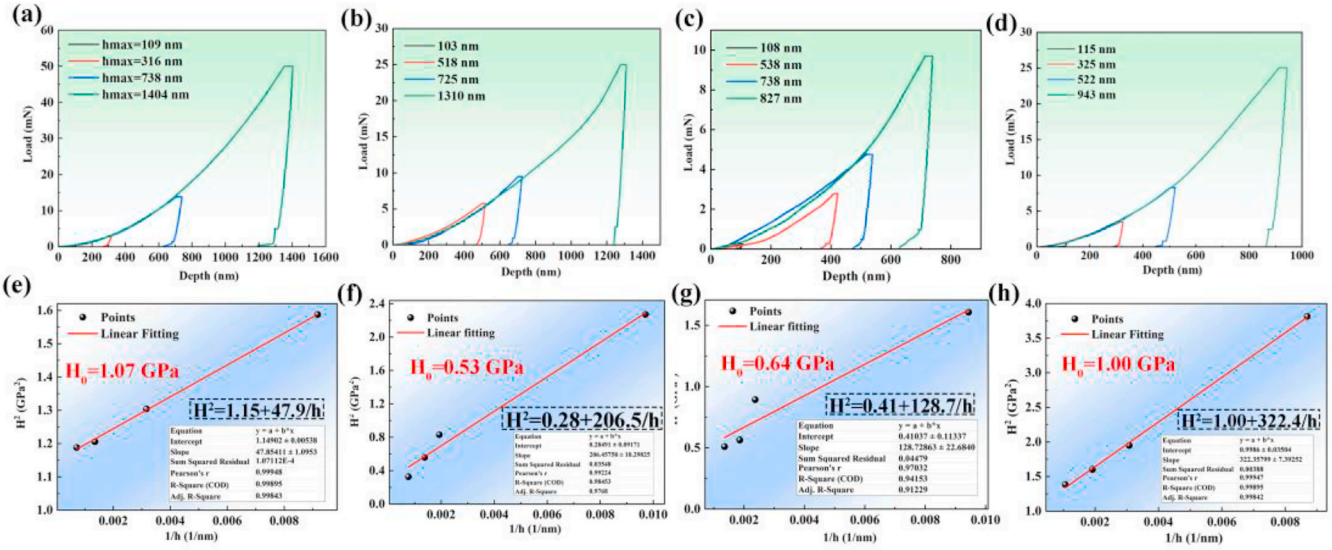


Fig. 9. (a)–(d) Representative nanoindentation *P-H* curves and (e)–(h) corresponding H^2-$1/h$ linear fitting plots at different indentation depths under TS.

for the 0-cycle region, the crack region, the high-porosity region, and the low-porosity region after 1500 cycles are calculated as 1.07 GPa, 0.53 GPa, 0.64 GPa, and 1.00 GPa, respectively. According to Eq. (15), the statistically stored dislocation densities (ρ_{SSDs}) for these regions are determined to be 2.98×10^{15} m^{-2},7.30×10^{14} m^{-2},1.06×10^{15} m^{-2}, and 2.60×10^{15} m^{-2}, respectively. It demonstrates that the 0-cycle die attach exhibits significantly higher ρ_{SSDs}. Following 1500 cycles of TS, the ρ_{SSDs} in the crack region, high-porosity region, and low-porosity region decrease by factors of 75 %, 64 %, and 13 %, respectively. It indicates that the pronounced reduction in ρ_{SSDs} in the crack and high-porosity regions is a major contributor to the severe deterioration in micro-mechanical performance. Furthermore, as summarized in Table 2, the ρ_{SSDs}, ρ_{GNDs}, and the total dislocation densities (ρ_{total}) reveal that, although ρ_{GNDs} tends to increase in regions exhibiting mechanical softening, the decline in ρ_{SSDs} outweighs the growth in ρ_{GNDs}. Consequently, ρ_{total} still exhibits a decreasing trend in areas with significant softening. Moreover, the ρ_{SSDs} in high-porosity area and crack area are significantly lower than those in low-porosity region. This indicates that the migration of pores and the coalescence of cracks are typically accompanied by a reduction in dislocation density, which can markedly degrade the local micromechanical properties.

In summary, the combined analysis of the microstructure and micromechanical properties indicates that regions experiencing pore migration and coalescence (i.e., high-porosity area and crack-initiated area) typically exhibit larger grain sizes, lower recrystallization fractions, and reduced dislocation densities. The die attach layer appears to undergo a "reverse sintering process," in which the crack regions formed by pore coalescence show a more pronounced grain coarsening, a sharper decrease in recrystallization fraction, and a more significant reduction in dislocation density. This behavior is primarily attributed to the thermal stresses that provide the driving force for pore migration and coalescence (as discussed in Section 4.2.1), which facilitates dislocation nucleation and motion and promotes grain growth. In addition, this process increases the intragranular misorientation, leading recrystallized grains to gradually evolve toward deformed grains and substructured grains. The repeated thermal shock accelerates the micro-mechanical degradation and eventual failure of the die-attach layer. Overall, our findings reveal that grain coarsening and the reduction in statistically stored dislocation density (ρ_{SSDs}) are the fundamental factors responsible for the degradation of the micro-mechanical properties in the sintered layer.

Table 2
Summary of dislocation densities.

	H_0/GPa	ρ_{SSD}/m^{-2}	ρ_{GND}/m^{-2}	ρ_{tot}/m^{-2}
0 cycle	1.07	2.98E+15	2.08E+14	3.18E+15
1500cycles_EBSD1	0.53	7.30E+14	9.43E+14	1.67E+15
1500cycles_EBSD2	0.64	1.06E+15	5.05E+14	1.57E+14
1500cycles_EBSD3	1.00	2.60E+15	4.66E+14	3.06E+15

4.2. Pore evolution mechanism and prediction

4.2.1. Mechanical behavior of pores evolution under TS

Due to the mismatch in the CTE among SiC, Ag, Cu, and Si_3N_4, the sintering layer undergoes heterogeneous deformation under alternating high and low temperature loading, resulting in stress concentration. This stress concentration, induced by cyclic loading, not only alters the microstructure characteristics of the sintered layer but also affects its mechanical properties. Furthermore, stress concentration can serve as a driving force for pore migration, crack initiation, and propagation. Therefore, it is essential to carry out the research of the micro-mechanical behavior simulation model for the sintered layer. The sintering layer, characterized by its porous structure, presents additional complexities, as the shape, location, and pore size significantly influence the residual stress distribution. Accurately constructing a porous model of the sintered layer is critical, as it directly determines the simulation precision and the data reliability. In this paper, a simulation model of the porous sintered layer was constructed based on SEM images of the porous morphology using MATLAB and subsequently imported into COMSOL Multiphysics for co-simulations. The workflow for converting SEM-observed pore morphologies into finite element (COMSOL) models is illustrated in Fig. 10. First, MATLAB was employed to process the SEM images and set parameters such as image dimensions and porosity. The images were binarized through the script, and the processed porosity was calculated. Next, the discrepancy between the target porosity and the automatically identified porosity was iteratively minimized until it fell within an acceptable threshold. Finally, the COMSOL simulation model was generated and exported. For the simulation, two representative regions were selected: the crack zone directly beneath the SiC die (after 1500 cycles) and the die edge region (before TS, 0 cycle). Based on the porous sintered layer models, SiC die and AMB substrate were proportionally added in COMSOL to simulate real operating conditions. Table 3 shows the list of the simulation material properties.

Fig. 11(a)–(d) illustrates the Von Mises stress distribution at two selected locations under environmental conditions of −45 °C and

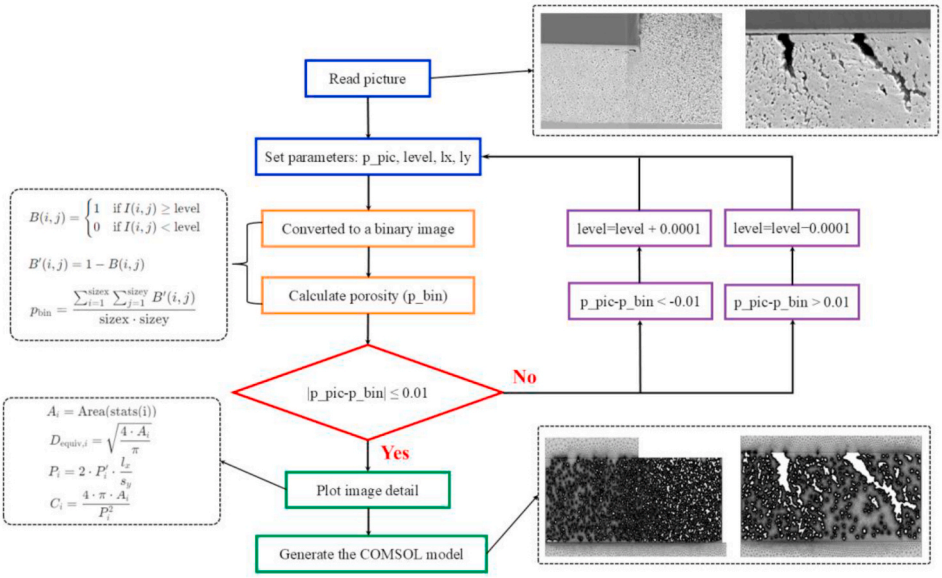


Fig. 10. Workflow illustrating the conversion of SEM-observed pore morphologies into finite element (COMSOL) models.

Table 3
Simulation material properties details.

Materials	Coefficient of thermal expansion (K^{-1})	Constant pressure heat capacity (J/(kg·K))	Density (kg/m^3)	Thermal conductivity (W/(m·K))	Young's modulus GPa	Poisson's ratio
Ag	1.89E-05	235	10500	450	70	0.37
SiC	4.30E-06	690	3216	390	400	0.45
Cu	1.70E-05	385	8960	400	110	0.35
Si3N4	2.30E-06	700	3100	60	300	0.23

125 °C, where the TS curve is shown in Fig. 11(i). Fig. 11(m1) and (m2) provide the stress distribution along the transverse direction for the 0-cycle sintered layer under −45 °C and 125 °C. It indicates that the mismatch in CTE leads to significantly higher stress at the interface between SiC die and die attach. The presence of two singularities in the stress distribution, caused by pore tips located near the interface in the model, is also noted. It can be observed that at −45 °C, the stress in the interior of the sintered layer beneath the SiC die is approximately 150 MPa, significantly higher than that in the sintered silver overflow region (approximately 85 MPa). At 125 °C, the stress in the sintered layer beneath the die increases to approximately 200–250 MPa, while the stress in the overflow region remains at around 140 MPa. Furthermore, under −45 °C and 125 °C, the stress in the sintered layer exhibits increased fluctuation near the die edges. It indicates that the mismatch in CTE leads to significantly higher stress at the interface between SiC die and die attach. As reported in earlier studies [40,41], the strength of die attach layer lies in the range of 200–350 MPa (sintering pressure >10 MPa, porosity = 6–14 %) at room temperature and around 150 MPa at 120 °C. Consequently, the relatively high interfacial stresses at the SiC die/sintered layer interface are expected to represent the most critical location for the onset of die-attach failure. Additionally, the stress in the sintered silver overflow region is notably lower than the stress beneath the die, with the highest stress observed at the sintered layer near the die edges.

Fig. 11(e)–(h) shows the volume strain distribution for two selected locations under environments of −45 °C and 125 °C. It can be observed that at both −45 °C and 125 °C, the volume strain at the interface between the SiC die and the sintered layer is the lowest, approximately −0.2 % and 0.3 %, respectively. Additionally, under the environment of −45 °C, the volume strain of the 0-cycle sintered layer beneath the SiC die is significantly lower than that in the overflow region (−0.35 %), as shown in Fig. (m3). Under the environment of 125 °C, the volume strain beneath the die in the sintered layer is approximately 0.3 %, markedly lower than that in the overflow region (0.55 %), as illustrated in Fig. (m4). Fig. 11(i) depicts the temperature-dependent volume strain variations around two randomly selected pores. It is evident that as the temperature transitions from −45 °C to 125 °C, the volume strain around the pores gradually shifts from shrinkage to expansion. However, the volume strain does not change after one cycle of the TS. It indicates that during the TS, the SiC die imposes constraints on the interconnection layer, hindering its free deformation and resulting in stress concentration at the interface. Conversely, the overflow region, which is not subjected to die-induced constraints, can freely expand and shrinkage, effectively releasing stress and alleviating significant stress concentration.

Fig. 11(j) illustrates the temporal evolution of average stress and average strain across the entire sintered layer region. It is evident that as the ambient temperature rises from −45 °C to 125 °C, the average stress of the sintered layer decreases progressively from an initial value of approximately 88 MPa. Subsequently, with the temperature further increasing to 125 °C, the average stress rises gradually, reaching approximately 140 MPa. Moreover, the average volume strain reveals a transition from −0.33 % at −45 °C to approximately 0.55 % at 125 °C. Table 3 highlights that the CTE of Ag is significantly higher than that of SiC. This disparity results in a larger strain in Ag compared to SiC at −45 °C. Consequently, SiC die constrains the volume contraction of the sintered layer, inducing tensile stress along the longitudinal direction. Similarly, at 125 °C, the mismatch in CTE causes the sintered layer to experience compressive stress. Notably, there are significant differences between the tensile and compressive stress values, as well as between the volume strain at −45 °C and 125 °C. These differences drive the coalescence of pores under TS.

Fig. 11(k) compares the stress distribution in the sintered layer, focusing on the two adjacent pores at 0 cycle and 1500 cycles. At −45 °C

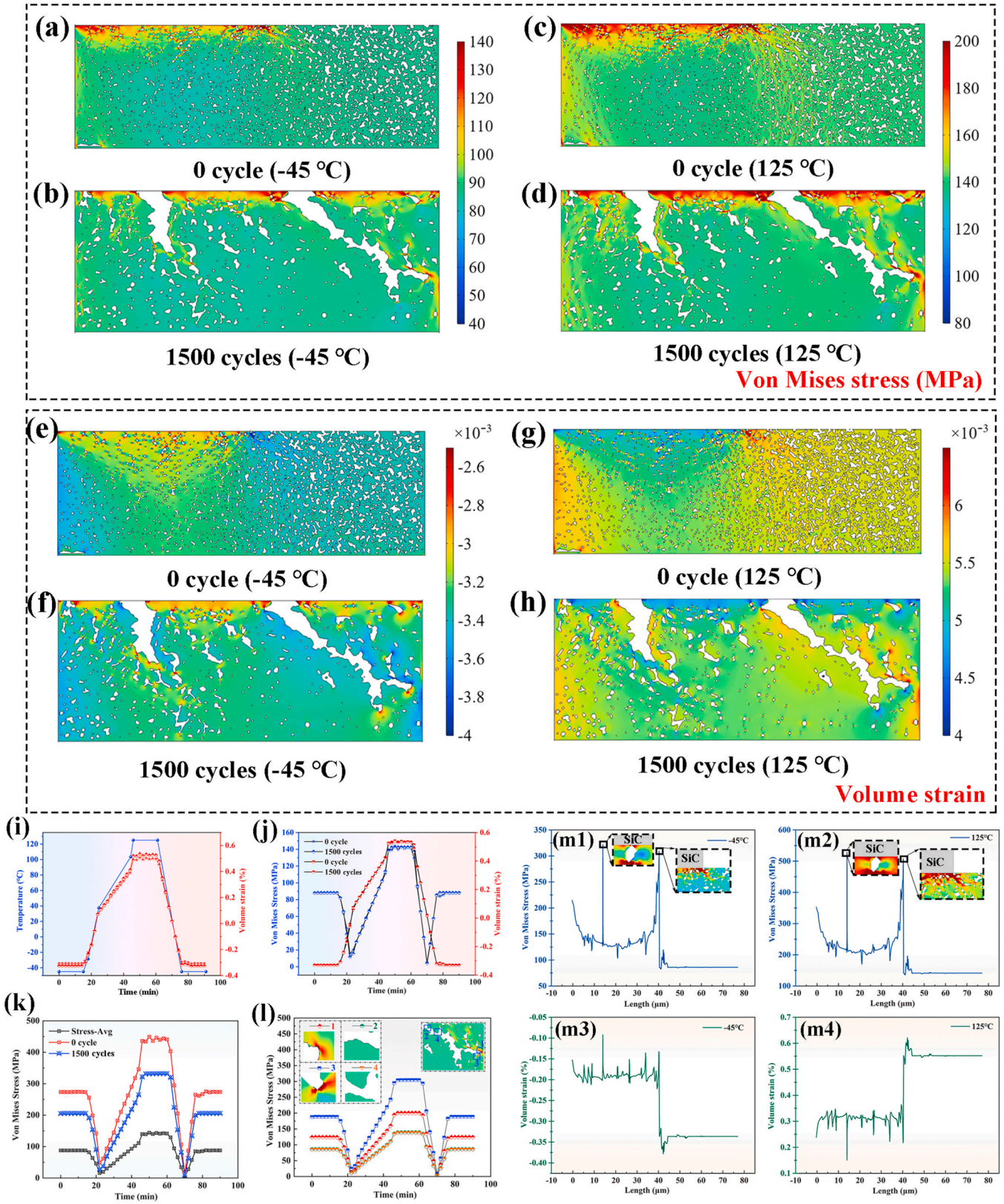


Fig. 11. Finite element simulation results of stress distribution in the sintered layer under TS: (a)–(d) Von Mises stress distribution, (e)–(h) volume strain distribution and (i)-(m4) their statistical plots.

and 125 °C, the stress values near the adjacent pores are approximately 274 MPa and 450 MPa at 0 cycle, respectively, reducing to around 204 MPa and 330 MPa after 1500 cycles. These findings indicate that the stress between adjacent pores is significantly higher than the average stress, providing a driving force for pore coalescence. Fig. 11(l) contrasts the stress distribution at the crack tip with its surrounding region. Regardless of whether the ambient temperature is −45 °C or 125 °C, the stress in the smoother transition regions around the crack is markedly lower than that at the irregular protrusions of the crack tip. It suggests that after cracks approach and merge, their irregular shapes exacerbate stress concentration at the crack tip. Under TS, this increased stress concentration accelerates the coalescence of adjacent pores.

In summary, due to the mismatch in CTE, the stress at the interface between the sintered silver layer and the SiC die is significantly higher

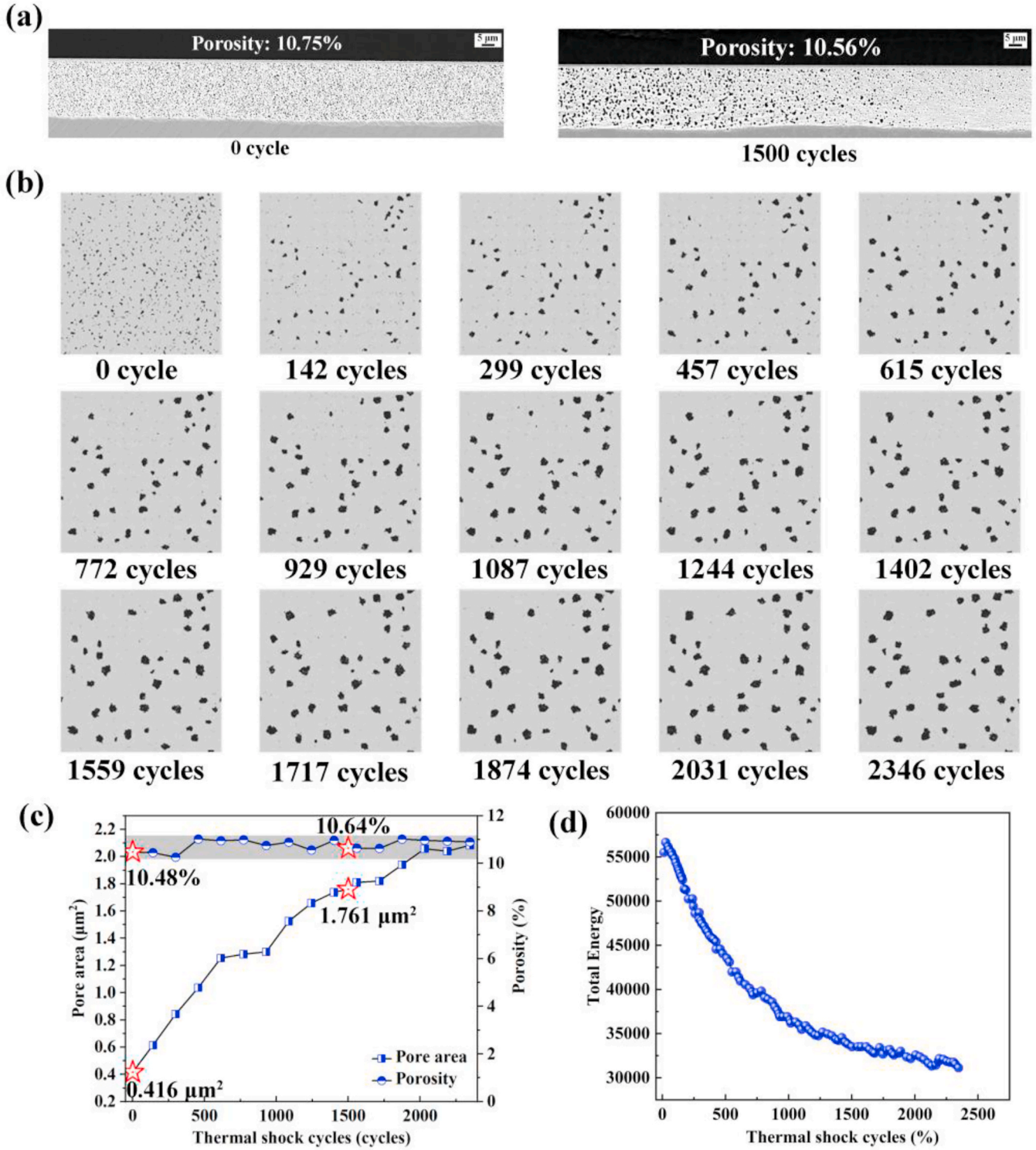


Fig. 12. Evolution and prediction of pore morphology in the sintered layer based on the KMC Potts model with Kawasaki dynamics: (a) experimental pore distributions at 0 cycle and 1500 cycles, (b) schematic illustration of pore evolution, (c) statistical evolution of pore size and porosity, and (d) system energy variation during TS.

than that in the interior, while the volume strain is noticeably lower. Particularly, the stress at the die edge increases markedly. The unequal tensile and compressive stresses induced by high and low temperature cycling provide a driving force for pore deformation and coalescence. Additionally, the irregular morphology of crack tips intensifies stress concentration, further accelerating the coalescence of neighboring pores.

4.2.2. Pores evolution prediction by KMC Potts model based on kawasaki dynamics

Based on the aforementioned results, the porosity in sintered layers undergoes migration, coalescence, and even crack formation during the TS. The morphology of the pores transitions from irregular, elongated shapes post-sintering to a more circular geometry. However, the transformation does not significantly affect the average porosity but instead induces a heterogeneous porosity distribution across the layer. To predict the long-term evolution of porosity under these conditions, the kinetic Monte Carlo (KMC) Potts model was employed. The Potts model, also known as the Q-state Potts model, has been extensively used to simulate grain growth, recrystallization, sintering, and diffusion behaviors in metals and ceramics [42–47]. In this study, the microstructure images were discretized into a regular lattice grid, where each pixel represents a lattice site denoted as q_i. All voids were assigned $q = 0$, while the sintered silver regions were designated as $q = 1$. Kawasaki dynamics were implemented to describe the diffusion process, wherein the states of two adjacent lattice sites were updated through exchange operations. This approach mimics the atomic exchange mechanisms inherent in diffusion while ensuring the conservation of the state variable throughout the system evolution [48]. The total system energy was expressed as:

$$E_{Potts} = \frac{1}{2}\sum_{i=1}^{N}\sum_{j=1}^{8} J_{ij}\left(1-\delta\left(q_i, q_j\right)\right) \tag{29}$$

where N denotes the total number of lattice sites in the system, with the number 8 representing the nearest-neighbor sites considered for a given lattice site i in the 2D grid. The matrix $J\ (q_i, q_j)$ defines the interaction energy between adjacent states, whether they represent silver or pore states. The probability of state transitions is governed by the Metropolis algorithm as follows:

$$P = \min\left(1, \exp\left(\frac{-\Delta E}{k_B T}\right)\right) \tag{30}$$

where ΔE represents the change in system energy before and after the exchange, $k_B T$ denotes the temperature of the simulated system. The algorithm ensures that the system evolves towards energy minimization, effectively modeling pore evolution. In the initial simulation setup, all interaction energies in the matrix J were set to 1, while the simulation temperature was set to 0.5. By aligning the time scale of the simulation cycles with experimental data, the pore area and porosity at 0 cycle and 1500 cycles were used as references, as shown in Fig. 12(c). By modifying the initial microstructural images or extending the number of simulation steps, this approach can predict pore evolution across a wider range of microstructures and longer cycles. These predicted images provide a valuable basis for further analysis of the electrical, thermal, and mechanical properties of the system.

Fig. 12 illustrates the evolution and prediction of pore morphology in the sintered layer based on the KMC Potts model of Kawasaki dynamics. Fig. 12(a) compares the experimental pore distribution in the sintered layer at 0 cycle and 1500 cycles. At 0 cycle, the pores are nearly homogeneously distributed, with a porosity of approximately 10.75 %. However, after 1500 cycles, the sintered layer exhibits a highly heterogeneous distribution, characterized by pore clustering and coalescence in the left region, while the pores in the right region have almost disappeared. Notably, the overall porosity remains nearly unchanged at approximately 10.56 %. Fig. 12(b) provides a visualization of the pore evolution behavior in the sintered layer predicted by the Kawasaki dynamics, where black regions represent pores. During TS, irregular strip-shaped pores progressively evolve into circular pores, aligning closely with experimental observations. The formation of strip-shaped pores is a result of external pressure, while their transformation into circular pores minimizes the system free energy, as illustrated in Fig. 12(d). Additionally, with an increasing number of cycles, partial pore disappearance and growth are observed, consistent with the migration and coalescence phenomena noted in experimental results. The average pore size demonstrates a approximate linear increase during this process, but the overall porosity distribution remains homogeneous at approximately 10.5 %, as shown in Fig. 12(c). In summary, the Potts model based on Kawasaki dynamics effectively characterizes the morphological evolution of pores and predicts their migration and coalescence, offering valuable insights into the pore evolution behavior of sintered layers under TS.

5. Conclusions

Research on the degradation mechanisms of die attach plays a crucial role in improving the reliability and optimizing pressureless sintering formulations. In this paper, the degradation mechanisms of silver sintered layers are explored using a multi-scale method that integrates experimental analysis, FEM and the Potts model based on Kawasaki dynamics. The main findings are as follows.

(1) The average porosity of the sintered layer remains unaffected by temperature shock, staying around 10 %. Nevertheless, after 1500 cycles, a clear alternating distribution of high and low porosity regions is observed, suggesting the migration and aggregation of pores. In addition, pore merging and crack formation are first observed near the die edges. The degradation of mechanical properties gradually loses its obstructive effect on pore migration.

(2) Following 1500 cycles, the grain size in the sintered layer undergoes non-uniform growth, with the grain sizes in the low porosity, high porosity, and crack regions increasing from an initial value of 0.37 μm–0.83 μm, 0.79 μm, and 1.05 μm, respectively. The fraction of recrystallized grains decreases significantly from 89.6 % to 37.3 %–72.1 %, accompanied by an increase in the average misorientation angle from 0.108° to 0.404°–0.745°. Despite a significant increase in the ρ_{GNDs}, especially in the crack region (approximately 9.4×10^{14} m^{-2}), the total dislocation density of the sintered layer decreases during the TS.

(3) The average hardness of the sintered layer decreases from 1.05 GPa to approximately 0.92 GPa after 1500 cycles, with hardness values exhibiting more discrete. Similarly, the average yield strength declines from approximately 326 MPa–231 MPa, with the crack zone and high-porosity region showing yield strengths as low as 103–117 MPa. The degradation of mechanical properties can be attributed to the growth of grain size and the reduction in dislocation density

(4) During TS, the mismatch in the CTE induces higher thermal stress concentration at the interface between the SiC die and the sintered layer, with the highest stress occurring at the edge of the interface. These thermal stresses serve as a driving force for pore migration, coalescence, and the initiation of cracks. Moreover, the irregular geometry at the crack tips tends to exacerbate the stress concentration, further accelerating the coalescence of adjacent pores and the propagation of cracks.

(5) Based on Kawasaki dynamics, the KMC Potts model effectively characterizes the transformation of irregular stripe-like pores into energetically more stable circular shapes under TS. Furthermore, it can characterize the migration and coalescence behavior of

pores at constant porosity and predict the pore size at a given cycle based on the approximate linear increase in pore size during TS.

CRediT authorship contribution statement

Chao Gu: Writing – original draft, Visualization, Investigation, Formal analysis, Data curation, Conceptualization. **Xiao Hu:** Writing – review & editing, Investigation. **Kai Lu:** Investigation, Funding acquisition. **Tao Wang:** Investigation, Funding acquisition. **Xuyang Yan:** Writing – review & editing. **Wei Chen:** Writing – review & editing. **Junwei Chen:** Writing – review & editing. **Xuejun Fan:** Supervision. **Guoqi Zhang:** Supervision. **Jiajie Fan:** Validation, Supervision, Resources, Project administration, Funding acquisition.

Code availability

The used code for the Kawasaki dynamics will be made on request. The used code for converting SEM morphology into finite element method models and converting load-displacement into stress-strain curve will be made on request.

Declaration of competing interest

The authors declare that they have no known competing financial interests or personal relationships that could have appeared to influence the work reported in this paper.

Acknowledgments

The work described in this paper was supported by the National Natural Science Foundation of China (Grant No. 52275559) and China Scholarship Council (Grant No. 202406100064).

Data availability

Data will be made available on request.

References

[1] C.W. Su, X. Yuan, R. Tao, M. Umar, Can new energy vehicles help to achieve carbon neutrality targets? J. Environ. Manag. 297 (2021) 113348.
[2] X. Yuan, X. Liu, J. Zuo, The development of new energy vehicles for a sustainable future: a review, Renew. Sustain. Energy Rev. 42 (2015) 298–305.
[3] J. Reimers, L. Dorn-Gomba, C. Mak, A. Emadi, Automotive traction inverters: current status and future trends, IEEE Trans. Veh. Technol. 68 (2019) 3337–3350.
[4] S.M.S.H. Rafin, R. Ahmed, M.A. Haque, M.K. Hossain, M.A. Haque, O. A. Mohammed, Power electronics revolutionized: a comprehensive analysis of emerging wide and ultrawide bandgap devices, Micromachines 14 (2023).
[5] K. Woo, Z. Bian, M. Noshin, R. Perez Martinez, M. Malakoutian, B. Shankar, S. Chowdhury, From wide to ultrawide-bandgap semiconductors for high power and high frequency electronic devices, JPhys Mater. 7 (2024).
[6] H. Yan, P. Liang, Y. Mei, Z. Feng, Brief review of silver sinter-bonding processing for packaging high-temperature power devices, Chinese, J. Electr. Eng. 6 (2020) 25–34.
[7] K. Wakamoto, T. Namazu, Mechanical characterization of sintered silver materials for power device packaging: a review, Energies 17 (2024).
[8] F. Hou, Z. Sun, M. Su, J. Fan, X. You, J. Li, Q. Wang, L. Cao, G. Zhang, Review of die-attach materials for SiC high-temperature packaging, IEEE Trans. Power Electron. 39 (2024) 13471–13486.
[9] R. Saccon, S.K. Bhogaraju, G. Elger, Cu sintering for high power electronics packaging - challenges and solutions, GMM-Fachberichte 105 (2022) 26–31.
[10] M. Wang, H. Zhang, X. Du, H. Yan, W. Hu, Y. Mei, Characterization of Multiple Commercial Sintered-silver Pastes as Die Attachment for Power Electronics Packaging: materials, Processing, and Properties, IEEE J. Emerg. Sel. Top. Power Electron. (2024) 1.
[11] L. Gao, X. Tian, C. Wu, Y. Xing, Y. Tan, X. Chen, G. Lu, Nano-Silver pressureless sintering technology in power module packaging, in: 2022 IEEE Int. Conf. Mechatronics Autom. ICMA, 2022, pp. 1452–1456, 2022.
[12] K. Son, A. Oh, E. Park, H.C. Bae, Thermal shock reliability of micro–nano bimodal Cu–Ag sintered joints, J. Mater. Sci. Mater. Electron. 33 (2022) 17493–17501.
[13] Y.G. Bongtae Han, Determination of an effective coefficient of thermal expansion of electronic packaging components: a whole-field approach, IEEE Trans. Compon. Packag. Manuf. Technol. 19 (1996) 240–247.
[14] V.K. Khanna, Adhesion-delamination phenomena at the surfaces and interfaces in microelectronics and MEMS structures and packaged devices, J. Phys. D Appl. Phys. 44 (2011).
[15] F. Yang, W. Zhu, W. Wu, H. Ji, C. Hang, M. Li, Microstructural evolution and degradation mechanism of SiC–Cu chip attachment using sintered nano-Ag paste during high-temperature ageing, J. Alloys Compd. 846 (2020) 156442.
[16] K.S. Siow, S.T. Chua, Thermal cycling of sintered silver (Ag) joint as die-attach material, Jom 71 (2019) 3066–3075.
[17] K. Wakamoto, T. Otsuka, K. Nakahara, T. Namazu, Degradation mechanism of pressure-assisted sintered silver by thermal shock test, Energies 14 (2021) 1–15.
[18] W.S. Hong, M.S. Kim, C. Oh, Y. Joo, Y. Kim, K.K. Hong, Pressureless silver sintering of silicon-carbide power modules for electric vehicles, Jom 72 (2020) 889–897.
[19] S.A. Zhang Z, C. Chen, Reliability of Ag Sinter-Joining Die Attach Under Harsh Thermal Cycling and Power Cycling Tests, J. Electron. Mater. 50 (2021) 6597–6606.
[20] L. Wang, Y. Ji, S. Li, P. Mei, Effect of particle shapes on thermal shock reliability of sintered Ag joints under low-temperature pressureless sintering, J. Mater. Eng. Perform. 32 (2023) 4427–4436.
[21] Z. Zhang, B. Wan, G. Fu, Y. Su, Z. Wu, X. Wang, X. Long, Impact analysis of microscopic defect types on the macroscopic crack propagation in sintered silver nanoparticles, C. - Comput. Model, Eng. Sci. 139 (2023) 441–458.
[22] C. Chen, H. Zhang, J. Jiu, X. Long, K. Suganuma, Thermal Fatigue Behaviors of Sic Power Module by Ag Sinter Joining Under Harsh Thermal Shock Test, China weld, vol. 31, English Ed., 2022, pp. 15–21.
[23] T. Herboth, M. Guenther, A. Fix, J. Wilde, Failure mechanisms of sintered silver interconnections for power electronic applications, Proc. - Electron. Components Technol. Conf. (2013) 1621–1627.
[24] K. Wakamoto, T. Otsuka, K. Nakahara, V. Mugilgeethan, R. Matsumoto, T. Namazu, Degradation Mechanism of Silver Sintering Die Attach Based on Thermal and Mechanical Reliability Testing, IEEE Trans. Compon. Packag. Manuf. Technol. 13 (2023) 197–210.
[25] N.A. Sakharova, J.V. Fernandes, J.M. Antunes, M.C. Oliveira, Comparison between Berkovich, Vickers and conical indentation tests: a three-dimensional numerical simulation study, Int. J. Solid Struct. 46 (2009) 1095–1104.
[26] K.O. Kese, Z.C. Li, B. Bergman, Method to account for true contact area in soda-lime glass during nanoindentation with the Berkovich tip, Mater. Sci. Eng. A 404 (2005) 1–8.
[27] J. Luo, J. Lin, A study on the determination of plastic properties of metals by instrumented indentation using two sharp indenters, Int. J. Solid Struct. 44 (2007) 5803–5817.
[28] X. Long, W. Tang, W. Xia, Y. Wu, L. Ren, Y. Yao, Porosity and Young's modulus of pressure-less sintered silver nanoparticles. 2017 IEEE 19th Electron. Packag. Technol. Conf. EPTC 2017 2018-Febru, 2017, pp. 1–8.
[29] S. Tu, X. Ren, J. He, Z. Zhang, Stress–strain curves of metallic materials and post-necking strain hardening characterization: a review, Fatig. Fract. Eng. Mater. Struct. 43 (2020) 3–19.
[30] M. Dao, N. Chollacoop, K.J. Van Vliet, T.A. Venkatesh, S. Suresh, Computational modeling of the forward and reverse problems in instrumented sharp indentation, Acta Mater. 49 (2001) 3899–3918.
[31] W.D. Nix, H. Gao, Indentation size effects in crystalline materials: a law for strain gradient plasticity, J. Mech. Phys. Solid. 46 (1998) 411–425.
[32] E. Song, M.T. Andani, A. Misra, Investigation of grain size and geometrically necessary dislocation density dependence of flow stress in Mg-4Al by using nanoindentation, Acta Mater. 265 (2024) 119633.
[33] C. Gu, X. Hu, X. Yan, W. Chen, J. Chen, K. Lu, T. Wang, G. Zhang, J. Fan, Interconnection mechanism and strengthening behavior of nano-silver sintered joints for silicon carbide power module packaging : a combined EBSD and nanoindentation study, J. Mater. Res. Technol. 38 (2025) 619–636.
[34] S. Graça, R. Colaço, P.A. Carvalho, R. Vilar, Determination of dislocation density from hardness measurements in metals, Mater. Lett. 62 (2008) 3812–3814.
[35] J. Carr, X. Milhet, P. Gadaud, S.A.E. Boyer, G.E. Thompson, P. Lee, Quantitative characterization of porosity and determination of elastic modulus for sintered micro-silver joints, J. Mater. Process. Technol. 225 (2015) 19–23.
[36] B.S.J. Kang, Z. Yao, E.J. Barbero, Post-yielding stress-strain determination using spherical indentation, Mech. Adv. Mater. Struct. 13 (2006) 129–138.
[37] A.G. Kostryzhev, Strengthening mechanisms in metallic materials, Metals 11 (2021).
[38] N. Hansen, Hall-petch relation and boundary strengthening, Scr. Mater. 51 (2004) 801–806.
[39] H. Conrad, K. Jung, Effect of grain size from millimeters to nanometers on the flow stress and deformation kinetics of Ag, Mater. Sci. Eng. A 391 (2005) 272–284.
[40] K. Wakamoto, Y. Mochizuki, T. Otsuka, K. Nakahara, Temperature dependence on tensile mechanical properties of sintered silver film, Materials 13 (2020) 4061.
[41] K. Wakamoto, Y. Mochizuki, T. Otsuka, K. Nakahara, T. Namazu, Tensile mechanical properties of sintered porous silver films and their dependence on porosity, Jpn. J. Appl. Phys. 58 (2019).
[42] W.E. Frazier, S. Hu, V.V. Joshi, A Potts Model parameter study of particle size, Monte Carlo temperature, and "Particle-Assisted Abnormal Grain Growth,", Comput. Mater. Sci. 185 (2020).
[43] H. Ko, J. Deng, I. Szlufarska, D. Morgan, Ag diffusion in SiC high-energy grain boundaries: kinetic Monte Carlo study with first-principle calculations, Comput. Mater. Sci. 121 (2016) 248–257.
[44] J.K. Mason, J. Lind, S.F. Li, B.W. Reed, M. Kumar, Kinetics and anisotropy of the Monte Carlo model of grain growth, Acta Mater. 82 (2015) 155–166.

[45] S.H. Oh, M. Lee, B.J. Lee, A full-scale Monte Carlo Potts model and real time conversion under non-uniform temperature distribution, Mater. Des. 225 (2023) 111439.
[46] Y. Zhang, X. Xiao, J. Zhang, Kinetic Monte Carlo simulation of sintering behavior of additively manufactured stainless steel powder particles using reconstructed microstructures from synchrotron X-ray microtomography, Results Phys. 13 (2019) 102336.
[47] S. Zhou, X. Liu, Z. Yan, S. Hara, N. Shikazono, Z. Zhong, Kinetic Monte Carlo (KMC) simulation of sintering of nickel oxide-yttria stabilized zirconia composites: model, parameter calibration and validation, Mater. Des. 232 (2023) 112094.
[48] J.A. Mitchell, F. Abdeljawad, C. Battaile, C. Garcia-Cardona, E.A. Holm, E. R. Homer, J. Madison, T.M. Rodgers, A.P. Thompson, V. Tikare, E. Webb, S. J. Plimpton, Parallel simulation via SPPARKS of on-lattice kinetic and Metropolis Monte Carlo models for materials processing, Model. Simulat. Mater. Sci. Eng. 31 (2023).